Theoretical and Applied Fracture Mechanics 127 (2023) 104039

Contents lists available at ScienceDirect

Theoretical and Applied Fracture Mechanics

journal homepage: www.elsevier.com/locate/tafmec

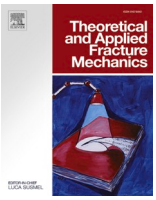

Extension of the peak stress method to estimate the fatigue limit of welded joints by means of the cyclic R-curve method

Luca Vecchiato [a], Mauro Madia [b], Giovanni Meneghetti [a,*]

[a] Department of Industrial Engineering, University of Padova, Via Venezia 1, 35131 Padova, Italy
[b] Bundesanstalt für Materialforschung und –prüfung (BAM), Division 9.4, D-12205 Berlin, Germany

ARTICLE INFO

Keywords:
Cyclic R-curve
Welded Joint
Fatigue Limit
Peak Stress Method
Finite Element Analysis

ABSTRACT

A new simplified and effective method has been formalised to estimate the Constant Amplitude Fatigue Limit (CAFL) of stress-relieved steel welded joints subjected to uniaxial push–pull loading and failing from the weld toe. Starting from the sharp V-notch assumption of the NSIF approach and the cyclic R-curve of the material in the heat affected zone, the proposed method identifies the CAFL as threshold level of the local stress field at the V-notched weld toe in the uncracked configuration. Such threshold stress field assures the crack arrest at the V-notched weld toe, according to the cyclic R-curve analysis. The method has been validated against experimental results and proved effective for a straightforward assessment of the CAFL of welded joints, as the stable crack propagation analysis of classical fracture mechanics approaches can be avoided.

1. Introduction

The strength of joints is a crucial aspect in ensuring the safety and structural durability of welded structures, as fatigue loading often leads to in-service failures at loads far below the static strength of the structure. One important parameter for designing steel welded structures is the fatigue limit, which theoretically represents the stress level below which an infinite number of constant amplitude loading cycles can be applied to the structure without the occurrence of any fatigue failure. When it comes to designing welded structures against fatigue, the nominal stress approach [1,2] is simple and widespread for industrial applications. This method starts by evaluating the applied nominal stress adopting standard solid mechanics-based stress calculations assuming a linear elastic material behaviour and ignoring any stress concentrations caused by the weld bead. The fatigue strength assessment is then performed by comparing the applied nominal stress to the fatigue strength of the joints, which is obtained directly from the Stress-Life (*S-N*) design curve chosen from a list of classified structural details [1,2].

Concerning the Constant Amplitude Fatigue Limit (CAFL), international standards and recommendations define the number of cycles at the knee point of the stress-life (*S-N*) design curve of the reference detail [1,2]. However, it varies depending on the standard (e.g. $5{\cdot}10^6$ cycles for Eurocode 3 [1], while 10^7 cycles for IIW recommendations [2]) indicating a lack of knowledge on this concept despite the significant implications it has on practical problems. Another limitation of the nominal stress approach arises when dealing with welded joints having complex geometrical features. In such case, [1,2] suggest conducting dedicated and often time-consuming experimental tests to determine the corresponding *S-N* curve, as the standard design curve for the specific geometry of the welded detail is not available in the list of classified structural details reported in [1,2].

On the other hand, the adoption of local approaches based on local rather than nominal quantities is advised by many studies in the literature [3,4], justified by the fact that metal fatigue is a localized process of crack initiation and propagation. In particular, it is known that the fatigue limit of sharply notched components (such as welded joints) is a fatigue crack propagation threshold phenomenon, a non-propagating crack being typically present at the notch tip when the applied stress level equals the fatigue limit [5–10]. In this scenario, damage tolerant approaches based on the principles of fracture mechanics [11] proved well suited to design structures against fatigue [12]. In more detail, the link between the fatigue limit and fracture mechanics is given by the fatigue crack propagation threshold ΔK_{th}, which represents the Stress Intensity Factor (SIF) range ΔK_I (i.e. maximum value minus minimum value, $K_{I,max}$ - $K_{I,min}$) below which long fatigue cracks stop propagating [11,12]. However, it is known that the crack propagation threshold depends on the crack length, where short cracks usually grow faster than long cracks when subjected to the same crack driving force, i.e., the same SIF range ΔK_I [12–15]. In particular, the fatigue crack propagation

* Corresponding author.
E-mail address: giovanni.meneghetti@unipd.it (G. Meneghetti).

https://doi.org/10.1016/j.tafmec.2023.104039
Received 21 June 2023; Received in revised form 29 July 2023; Accepted 1 August 2023
Available online 5 August 2023

Nomenclature

a	Crack length
a_0	Reference crack length for DCPD measurement
a_{CPC}	Crack length after Compression Pre-Cracking (CPC)
a_i	Initial crack length
a_{PSM}	Reference geometrical dimension according to the PSM
a_{PSM}/d	Mesh density ratio
A	Cross-sectional area of the main plate
c/a	Elliptical crack aspect ratio
c_{w1}	Coefficient accounting for mean stress effect according to PSM
d	Global size of the finite elements
Δ	Range of cyclic quantities (maximum minus minimum)
$\Delta a = a - a_{CPC}$	Crack length increment
ΔF	Axial force range
ΔK_I	Stress Intensity Factor (SIF) range
$\Delta K_I\,(a)$	Driving force, i.e. applied SIF dependence on crack length
$\Delta K_{I,\Delta\sigma 0}\,(a)$	Driving force at the plain material fatigue limit
$\Delta K_{I,\Delta\sigma g,th}\,(a)$	Driving force at the component fatigue limit
$\Delta K_{th}(\Delta a)$	Fatigue crack propagation threshold dependence on crack size (cyclic R-curve)
$\Delta K_{th,LC}$	Fatigue crack propagation threshold for long cracks
$\Delta K_{th,eff}$	Intrinsic component of the fatigue crack propagation threshold
$\Delta K_{th,op}$	Closure-induced component of the fatigue crack propagation threshold
ΔK_1^V	Notch Stress Intensity Factor (NSIF) range
$\Delta K_{1,th}^V$	Threshold NSIF
$\Delta\sigma_0$	Plain material fatigue limit
$\Delta\sigma_{eq,peak}$	Equivalent peak stress based on the PSM
$\Delta\sigma_{eq,peak,th}$	Threshold value of the equivalent peak stress
$\Delta\sigma_{FAT,IIW}$	FAT class of the reference detail according to IIW recommendations
$\Delta\sigma_{FAT,EC3}$	FAT class of the reference detail according to Eurocode3
$\Delta\sigma_g$	Range of the gross nominal stress
$\Delta\sigma_{g,th}$	Component fatigue limit
ΔV	Measured potential drop
ΔV_0	Reference the potential drop
$\Delta\overline{W}_1$	Averaged Strain Energy Density (SED) range
$\Delta\overline{W}_{1,th}$	Threshold averaged SED range
e_1	Coefficient for evaluating $\Delta\overline{W}_1$
E	Young's modulus
f_{w1}	Coefficient for calculating $\sigma_{eq,peak}$
H	Height of the specimen
I	Magnitude of the electrical current
K_{FE}^*	Non-dimensional NSIF parameter based on PSM
l_i	Fictitious length scales used to fit the cyclic R-curve
λ_1	Stress singularity degree
N_f	Number of cycles to failure
ν	Poisson's ratio
ν_i	Weight factors used to fit the cyclic R-curve
$R = (\sigma_{min}/\sigma_{max})$	Load ratio
R_0	Size of material structural volume according to SED criterion
ρ	Notch tip radius
r, θ, z	Coordinates of cylindrical reference system at notch tip
σ_g	Gross nominal stress
$\sigma_{rr}, \sigma_{\theta\theta}, \tau_{r\theta}$	In-plane stress components in cylindrical coordinate system
$\sigma_{\theta\theta,\theta=0,peak}$	Linear elastic peak stress calculated by FEA according to PSM
$\bar{\sigma}_{\theta\theta,\theta=0,peak}$	Averaged peak stress
t	Main plate thickness
W	Width of the specimen
y	Distance of the potential probe from crack plane

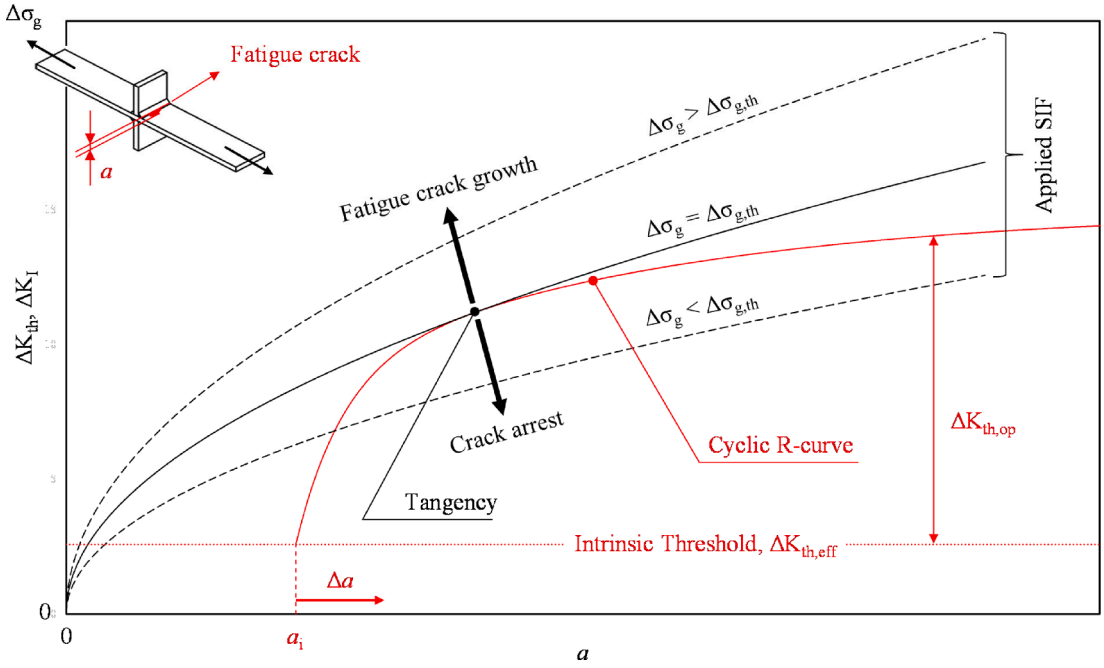

Fig. 1. Schematic of the cyclic R-curve analysis applied to a welded joint.

threshold ΔK_{th} of short cracks is lower than for long cracks $\Delta K_{th,LC}$, due to the gradual build-up of the crack closure [13,14,16–18]. In more detail, the fatigue crack propagation threshold consists of both an intrinsic component $\Delta K_{th,eff}$, depending on the lattice and elastic properties of the material [12,19,20], and of a closure-induced component $\Delta K_{th,op}$, which changes as the closure phenomena evolve until the long crack regime is achieved [12]. Such evolution of the fatigue crack propagation threshold for physically/mechanically short cracks can be described using the cyclic R-curve concept [12,14,15,21–25].

The fatigue limit of a cracked component can be determined by performing the so-called cyclic R-curve analysis (Fig. 1) [14,21,24,26]. Similar to the well-established monotonic R-curve analysis, this procedure consists in comparing the driving force of a propagating crack (black lines in Fig. 1), which mainly depends on geometry and external loads ($\Delta\sigma_g$ in Fig. 1), with the relevant resistance curve (red line in Fig. 1), i.e. the cyclic R-curve. The crack propagation occurs whenever the crack driving force is higher than the resistance one, while the crack is arrested in the opposite case. Consequently, the fatigue limit $\Delta\sigma_{g,th}$ is the maximum applicable stress level at which crack arrest is possible and typically results in the crack driving force to be tangent to the resistance curve (solid black line in Fig. 1).

The cyclic R-curve analysis is effective in estimating the fatigue limit [25,27,28] but its rigorous application is a complex task as it requires time and expertise both in measuring the material properties of short cracks, i.e. the cyclic R-curve, and in evaluating the driving force, i.e. the applied stress intensity factor for a range of (short) crack lengths. Although the applied SIF can be evaluated through analytical expressions available for simple geometries (e.g. [2,29–32]), FE calculations are necessary for treating more complicated design situations. FE simulations require the local weld bead geometry (weld leg size z, weld toe and weld root radius ρ, opening angle 2α, etc.) as well as the location, path and shape of the propagating crack to determine the corresponding SIF values. As a result, both modelling effort and computational time for complex geometries can be significant, as short cracks must be incorporated into large and tightly meshed geometries. Thus, those limitations clearly represent a hindrance in many industrial applications where the analysed structures are large, have many welded connections, and complex joint geometries.

In light of the above, the present analysis proposes an effective and straightforward assessment of the constant amplitude fatigue limit of welded structures with weld toe failure. The novel procedure consists in a combination of the cyclic R-curve analysis and the Peak Stress Method (PSM), an engineering tool that uses linear elastic finite element analyses to quickly assess the fatigue strength of welded structures [33,34]. It is important to underline that this methodology represents an important extension of the PSM to the infinite life regime. In fact, until now the PSM did not incorporate explicitly the fatigue limit [35]. More in detail, the concept of Notch Stress Intensity Factor (NSIF) ΔK_1^V, representing the intensity of the local linear elastic stress field at the weld toe, is exploited along with the cyclic R-curve analysis to define the fatigue limit of welded structures in terms of a threshold value for the NSIF $\Delta K_{1,th}^V$. This way, the CAFL is expressed as the threshold level of the local stress field at the weld toe in the uncracked configuration, which implicitly takes into account the arrest condition of a propagating crack according to the cyclic R-curve analysis. Then, the obtained NSIF at threshold $\Delta K_{1,th}^V$ is translated into the equivalent peak stress at threshold $\Delta\sigma_{eq,peak,th}$ and included in the fatigue design curve of the Peak Stress Method.

The case of weld toe failure of stress-relieved welded joints made of S355J2 + N structural steel under pure mode I fully reversed (R = -1) cyclic loading has been considered. The cyclic R-curve has been determined experimentally for the Base Material (BM) and also for the material in Heat Affected Zone (HAZ). Eventually, the novel procedure has been validated reanalysing experimental data relevant to four different test series taken from the literature.

2. The novel approach to estimate the fatigue limit of welded joints

2.1. The cyclic R-curve analysis

The cyclic R-curve analysis allows to estimate the fatigue limit of a component $\Delta\sigma_{g,th}$ by scaling the driving force $\Delta K_I(a)$ (the applied stress intensity factor vs crack length function), until the tangency condition is found with the resistance curve $\Delta K_{th}(a)$ (the cyclic R-curve), as depicted in Fig. 1. Considering the S355J2 + N structural steel analysed in the present investigation, the cyclic R-curve has been experimentally determined both for the Base Metal (BM) and the Heat Affected Zone (HAZ), the latter being interesting since crack initiation and early crack growth phases in welded joints occur within the HAZ. Accordingly, two different batches of Single Edge Notch in Bending (SENB) have been used. The first batch consisted of specimens made of Base Metal (BM, Fig. 2a), while the second was made from a transverse loaded K-groove butt weld ground flush to plate (HAZ, Fig. 2b); in all cases residual stresses have been relieved by post-weld heat treatment. The crack starter notch has been realized by electrical-discharge machining, which was made inside the HAZ for the second batch of specimens to investigate the propagation within this region (Fig. 2c).

Specimens have been loaded in pure bending at a load ratio R = -1 using a RUMUL TESTRONIC 100kN and a RUMUL TESTRONIC 20kN resonance-testing machines having working frequency of approximately 60 Hz and 108 Hz, respectively. The negative load ratio was possible thanks to an eight-point-bending device for SENB specimens, which allowed the application of fully reversed pure bending cyclic loading (Fig. 3a, b, and d). More precisely, during the fatigue crack growth tests the test machine has been closed-loop controlled in terms of applied force or applied SIF range ΔK_I, the latter being calculated adopting the equation reported into the standard ISO12108:2018 [36]:

$$K_I = \frac{F}{WH^{1/2}} \cdot \frac{S_{max} - S_{min}}{2H} \cdot 3 \cdot \sqrt{2\tan\frac{\pi a}{2H}} \cdot \left[\frac{0.923 + 0.199\left(1 - \sin\frac{\pi a}{2H}\right)^4}{\cos\frac{\pi a}{2H}} \right] \quad (1)$$

where F is the applied force, W and H are the width and the height of the specimen, respectively, a is the crack length, while S_{max} and S_{min} are major and minor spans of the 8-point-bending fixtures, respectively, as reported in Fig. 3a.

In-situ real-time crack growth monitoring has been performed using the Direct Current Potential Drop (DCPD) method illustrated in Fig. 3a, c, and d [22,37]. The DCPD technique is based on the increase of electrical resistance following the reduction of the cross section of the specimen due to crack growth. Therefore, according to Ohm's law, the increase of the electrical resistance translates into an increase of the potential drop, the specimen being subjected to a constant electrical current flow. Then, the crack depth is estimated by entering the experimentally measured potential drop into a proper calibration curve. In case of SENB specimens, the following analytical expression for the DCPD calibration curve is available [38]:

$$a = \frac{2H}{\pi} \cdot \arccos \frac{\cosh\frac{\pi y}{2H}}{\cosh\left[\frac{\Delta V}{\Delta V_0} \cdot \operatorname{acosh}\left(\frac{\cosh\frac{\pi y}{2H}}{\cos\frac{\pi a_0}{2H}}\right)\right]} \quad (2)$$

where a is the crack length, ΔV the measured potential, H the specimen height, y the distance between the potential probes and the crack plane, while ΔV_0 and a_0 are the potential drop measured before applying fatigue loads and the notch depth, respectively (Fig. 3a and d). A DC Power Supply HP6033A equipped with a pole-switcher has been employed to inject the DC current (I = 4 A) through the specimen and to change the current flow direction in order to compensate the thermoelectric effects [37]. Then, a Keithley 2182A Nanovoltmeter has been used to measure the potential drop signal (Fig. 3c). Finally, the effect of temperature variations on the measured potential drop has been

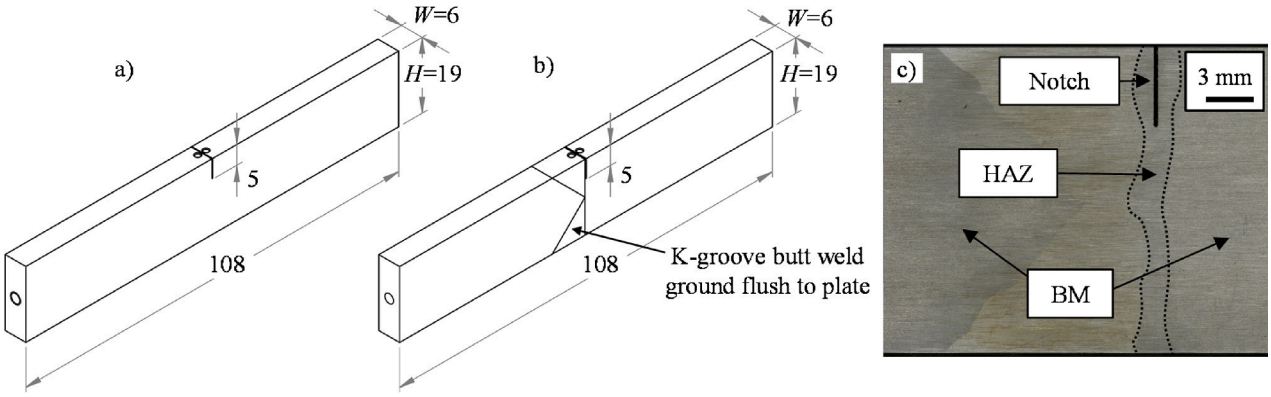

Fig. 2. SENB specimens made of: a) S355J2 + N, b) welded S355J2 + N, with the EDM notch inside the HAZ, c) macrograph of a welded specimen showing the EDM notch location.

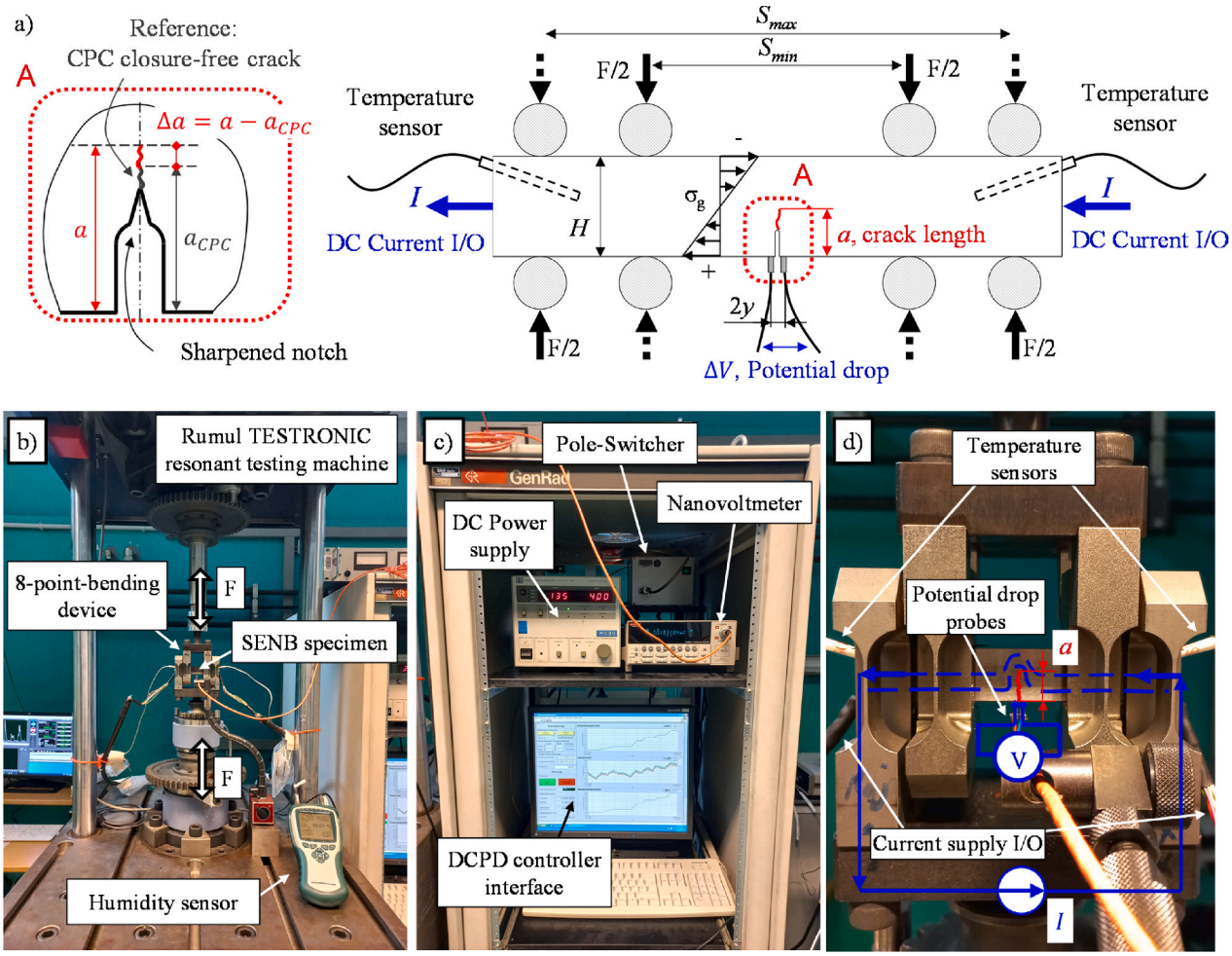

Fig. 3. Experimental setup used to determine the cyclic R-curve with a load ratio R = -1: a) schematic of the experimental setup, b) picture of the testing machine and c) of the DCPD device, d) with a focus on the 8-point-bending fixture and the DCPD equipment.

compensated by real-time monitoring the temperature of the specimen and by taking advantage of the linear correlation between the electrical resistivity of the material and the temperature [39,40].

The procedure adopted by Tabernig and Pippan [22] and recently updated by Pourheidar et al. [25] has been used to evaluate the cyclic R-curve. Accordingly, a closure free crack has been generated at the notch tip by applying a standard compression pre-cracking procedure in bending with a load ratio R = 20 and using an initial $\Delta K_I = 16$ MPa·m$^{0.5}$, the value being based on previous experience [22,25,41,42]. After compression pre-cracking, the specimen has been loaded under fully reversed ($R = -1$) constant amplitude bending at a load level close to the intrinsic threshold $\Delta K_{th,eff}$. At this stage constant ΔF procedure has been used. If no propagation occurred, the load range has been increased of about 0.5–1 MPa·m$^{0.5}$ (~$0.1 \cdot \Delta K_{th,LC}$ [22,25]). At a SIF range level high enough to trigger crack propagation, closure phenomena built up and after a certain extension the crack arrested. Then, the load has been

increased and the procedure repeated until no crack arrest has been observed. At this point the test has been interrupted and the upper part of the cyclic R-curve has been determined by increasing stepwise the applied SIF range ΔK_I. Eventually, at a given $\Delta K_I > \Delta K_{th,LC}$ the crack did not arrest and a further constant ΔF procedure has been started to describe the long crack propagation curve. The cyclic R-curve has been obtained by connecting the arrest points, defined as the crack length increments from the initial closure-free crack to each current crack arrest $\Delta a = a - a_{CPC}$ (where a_{CPC} is the size of the crack after the compression pre-cracking phase, see Fig. 3a) with the corresponding stress intensity factor range ΔK_{th}. Results of the performed tests are reported in Fig. 4 both for the BM (black dots in Fig. 4) and the HAZ (red dots in Fig. 4). Interestingly, Fig. 4 highlights there are no significant differences between BM and HAZ for crack increments smaller than $\Delta a < 0.5$ mm, with the difference being evident, on the other side, for longer cracks ($\Delta a > 0.5$ mm, Fig. 4).

Finally, experimental data have been fitted using the following expression (Maierhofer et al. [43]):

$$\Delta K_{th} = \Delta K_{th,eff} + \left(\Delta K_{th,LC} - \Delta K_{th,eff}\right)\cdot\left[1 - \sum_{i=1}^{n} \nu_i \cdot e^{-\frac{\Delta a}{l_i}}\right] \quad (3)$$

where l_i are length-scale parameters based on the physical idea that each crack closure mechanism requires a certain crack extension to build up completely, while ν_i are weights which satisfy the following condition:

$$\sum_{i=1}^{n} \nu_i = 1 \quad (4)$$

The best fit has been performed taking advantage of the curve fitting tool implemented in Matlab® by imposing $i = 2$ and the resulting parameters are $\nu_1 = 0.495$, $l_1 = 0.046$ mm, $\nu_2 = 1 - \nu_1 = 0.505$, $l_2 = 1.913$ mm, $\Delta K_{th,eff} = 2.53$ MPa·m$^{0.5}$, $\Delta K_{th,LC} = 10$ MPa·m$^{0.5}$, the latter value being in good agreement with [44]. The corresponding curve is shown as a solid red line in Fig. 4.

The next step consists in defining the initial crack size a_i (see Fig. 1) to fully compute the resistance force. In this investigation, the criterion used in IBESS [26,29,30,45] has been adopted, although many different proposals have been put forward in the literature (the reader is referred to the recent review on this topic [26]). According to this criterion, the initial crack size a_i is obtained by performing a crack arrest analysis, consisting in comparing the driving force $\Delta K_{I,\Delta\sigma 0}(a)$ at the fatigue limit for smooth specimens (the plain material fatigue limit) with the cyclic R-curve $\Delta K_{th}(a)$. In more detail, the driving force $\Delta K_{I,\Delta\sigma 0}(a)$ is referred to a semi-circular surface crack propagating normal to the load direction in a plain specimen under fully reversed ($R = -1$) axial cyclic loading at a stress range equal to the plain material fatigue limit $\Delta\sigma_0$. Then, the initial crack size a_i is obtained by shifting the cyclic R-curve along the abscissa until the tangency condition is achieved with the driving force, with the cyclic R-curve being fixed along the ordinate but not along the abscissa. Zerbst et al. [45] found an initial crack size $a_i = 17$ μm for a S355NL structural steel by means of the crack arrest analysis just discussed. Note that, according to the same authors, the largest crack-like defect (e.g. non-metallic inclusions, pores, cavities, shrinkages, weldments defects, microcracks, surface roughness, undercuts, corrosion pits, scratches, …) should be used as initial crack when its size is larger than a_i obtained from the crack arrest analysis [45].

2.2. Threshold notch stress intensity factor $\Delta K^V_{I,th}$

After determining the initial crack size a_i with the resistance curve $\Delta K_{th}(a)$, the fatigue limit of the welded joint $\Delta\sigma_{g,th}$ (the component fatigue limit) is found by scaling the driving force $\Delta K_I(a)$ until the tangency condition is achieved with the resistance curve, the position of the latter being fixed by a_i, according to the concept illustrated in Fig. 1. Generally speaking, estimating the applied stress intensity factor (SIF) is a complex task, since it requires to know the local weld bead geometry and the location, path and shape of the propagating crack, which can be challenging and possibly requiring the use of complex crack propagation algorithms and estimations [46,47]. Moreover, as discussed above, even if simplified approaches exist for some simple cases [2,29–32], computation times to determine the value of $K_I(a)$ for complex geometries can be significant, as short cracks must be incorporated into large and tightly meshed geometries, requiring multiple analysis for different values of a.

In the present investigation, the following simplifying assumptions have been introduced to calculate the driving force:

- Null weld toe radius, $\rho = 0$.
- Crack propagating along the V-notch bisector line.
- Through-the-thickness straight-fronted planar crack.

In agreement with the worst-case concept [15,48–50], the assumption of a null weld toe radius arises from observing that its real value is

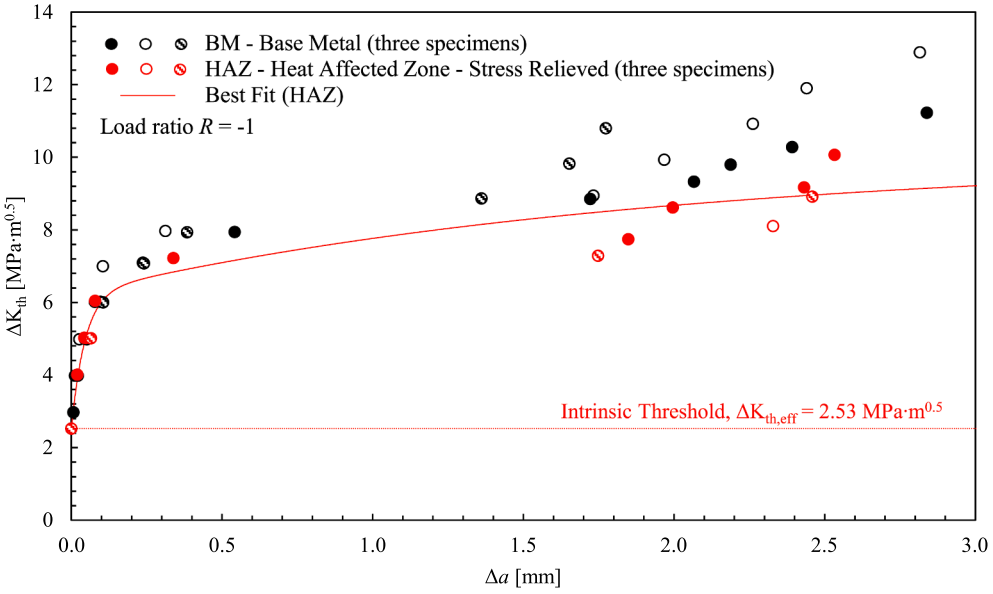

Fig. 4. Experimental cyclic R-curves of BM and HAZ specimens with the curve fitted on HAZ data. The markers' different filling identifies different specimens from the same batch.

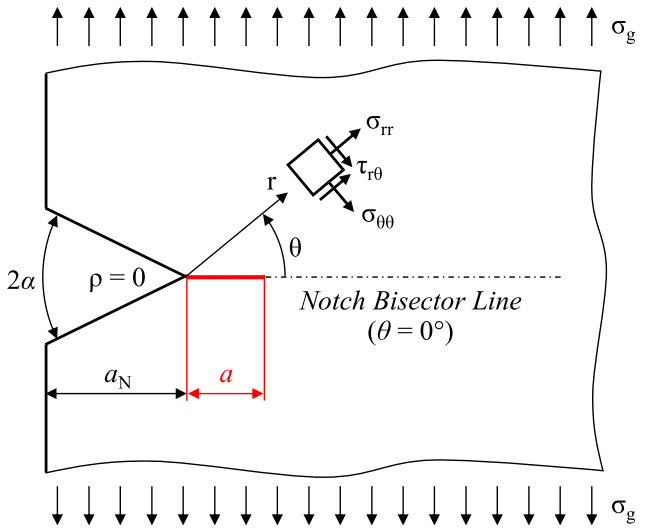

Fig. 5. Cylindrical coordinate system (r, θ, z) centered at the sharp V-notch tip (2α, $\rho = 0$) and local stress components in a plane problem. The red line is the through-the-thickness straight-fronted crack propagating along the notch bisector line.

often very small for arc-welded joints and hence the weld toe is modelled as a sharp V-notch having null tip radius ($\rho = 0$) and opening angle $2\alpha = 135°$ (see Fig. 5). As a consequence of the null tip radius, a singular stress field is produced at the weld toe by the external loads, the stresses being proportional to $1/r^{1-\lambda 1}$ [51], where r is the radial distance from the V-notch tip (Fig. 5) and the singularity degree ($1-\lambda_1$) is a function of the opening angle [51,52]. In the framework of linear elasticity, the singular stress field is proportional to the external loads and its intensity is quantified by the Notch Stress Intensity Factor (NSIF) K_1^V [53], which represents the natural extension of the SIF K_I concept to sharp notches having opening angle $2\alpha > 0°$. The NSIF K_1^V is defined according to Eq. (5) and it has been extensively demonstrated that its range ΔK_1^V can be used to correlate the fatigue strength of welded joints having different geometries and absolute dimensions [49,50].

$$K_1^V = \sqrt{2\pi}\cdot\lim_{r\to 0}\left[\sigma_{\theta\theta}(r,\theta=0)\cdot r^{1-\lambda_1}\right] \tag{5}$$

Interestingly, the NSIF concept can be very useful to determine the SIF K_I of short cracks propagating along the bisector line of a sharp V-notch. Indeed, the stress field of the cracked configuration is completely determined by the stress field of the un-cracked configuration (i.e. by the NSIF K_1^V) and can be evaluated using the following engineering formula [31,54–61]:

$$\Delta K_I = C_{2\alpha}\cdot\sqrt{\pi}\cdot a^{\lambda_1-0.5}\cdot\Delta K_1^V \tag{6}$$

where $C_{2\alpha}$ is a constant parameter depending on the V-notch opening angle 2α, a is the crack length measured from the V-notch tip (see Fig. 5), λ_1 is the Williams' singularity exponent [51,52] and ΔK_1^V is the NSIF quantifying the intensity of the asymptotic stress distribution ahead of the sharp V-notch tip of the uncracked configuration. The geometric factor $C_{2\alpha}$ can be evaluated using FE simulations or using some analytical expressions available in the literature, the latter being valid in case of a through-the-thickness straight-fronted planar crack propagating along the bisector line of a sharp (or rounded) V-notch [31,54–61]. For example, Atzori et al. [61] proposed the following expression:

$$C_{2\alpha} = -4.658\cdot10^{-6}\cdot(2\alpha)^2 + 1.840\cdot10^{-4}\cdot(2\alpha) + 5.629\cdot10^{-1} \tag{7}$$

where 2α is expressed in degrees.

Since the case of weld toe failure of stress-relieved welded joints made of S355J2 + N structural steel under pure mode I fully reversed ($R = -1$) cyclic loading is considered (see Fig. 6), the opening angle has been fixed to $2\alpha = 135°$ ($\lambda_1 = 0.674$ [51,52]) and the driving force has been evaluated for different crack lengths a ranging from 0 to 500 μm by means of Eq. (6), wherein $C_{2\alpha} = 0.503$ (Eq. (7)) has been used. Eventually, the driving force (Eq. (6)) has been scaled by changing the value of ΔK_1^V and the tangency was found for a threshold value of the NSIF range equal to $\Delta K_{1,th}^V = 32.8$ MPa·m$^{0.326}$ (Fig. 6). The obtained parameter allows to rapidly design welded structures against fatigue in the infinite life region. Indeed, its most significant advantage is that it estimates the fatigue strength of complex structures by analysing only the intensity of the local asymptotic stress field at the weld toe. Accordingly, the arrest condition of a propagating crack given by the cyclic R-curve results into a threshold value for the local stress field at the weld toe in the uncracked configuration. This is possible thanks to the NSIF ΔK_1^V range, which summarizes all pieces of information on geometry, dimensions, applied loads and boundary conditions (e.g. axial or bending) into a single stress parameter. Whenever the applied NSIF is higher than the threshold value, i.e. $\Delta K_1^V > \Delta K_{1,th}^V$, then the welded detail is subjected to a stress level higher than its fatigue limit (or in other words the driving force will never meet the resistance curve, see Fig. 1 and Fig. 6). Otherwise, if $\Delta K_1^V \le \Delta K_{1,th}^V$ the corresponding applied stress is lower than or equal to the component's fatigue limit.

2.3. The peak stress Method: Definition of the constant amplitude fatigue limit $\Delta\sigma_{eq,peak,th}$

Among approaches exploiting the NSIF concept to assess the fatigue strength of welded joints, the averaged Strain Energy Density (SED) [62] criterion deserves a mention. Based on the notch sensitivity observations raised by Neuber [63], it assumes the local Strain Energy Density (SED) $\Delta\overline{W}$ averaged over a finite material structural volume as fatigue damage parameter. In more detail, Lazzarin and Zambardi [62] suggested to evaluate the averaged SED $\Delta\overline{W}$ in a circular-shaped material structural volume surrounding the weld toe (the latter being modelled as sharp V-notch, see Fig. 7a) and having radius $R_0 = 0.28$ mm for arc-welded structural steel joints [64] (see Fig. 7b). Assuming an isotropic linear-elastic material behaviour under plane strain conditions along with the Beltrami total strain energy criterion [65], the range of the average SED for a sharp V-notch under pure mode I loading $\Delta\overline{W}_1$ can be written as a function of the mode I NSIF range ΔK_1^V as follows [62]:

$$\Delta\bar{W}_1 = c_{w1}\frac{e_1}{E}\left(\frac{\Delta K_1^V}{R_0^{1-\lambda_1}}\right)^2 \tag{8}$$

where E is the Young's modulus of the material (here assumed to be $E = 206000$ MPa), e_1 is a coefficient depending on the sharp V-notch opening angle 2α and the Poisson's ratio ν (here assumed to be $\nu = 0.3$) [62], while c_{w1} accounts for the mean stress sensitivity in case of stress-relieved joints. A parametric polynomial expression has been recently introduced to compute the total SED coefficient e_1 for a generic V-notch opening angle 2α and Poisson's ratio ν [52] and its value equals $e_1 = 0.117$ at the weld toe of steel arc-welded joints ($2\alpha = 135°$, $\nu = 0.3$). While c_{w1} is forced to $c_{w1} = 1$ for as-welded joints due to the residual stress state [34], for stress-relieved joints c_{w1} is defined as a function of the nominal load ratio $R = (\sigma_{g,min}/\sigma_{g,max})$ according to the following expression [50]:

$$c_{w1}(R) = \begin{cases} \dfrac{1+R^2}{(1-R)^2} & if \quad stress-relieved \quad and \quad -1 \le R \le 0, \\ \dfrac{1-R^2}{(1-R)^2} & if \quad stress-relieved \quad and \quad 0 \le R < 1, \\ 1 & if \quad as-welded \quad for \quad any \quad R \quad value \end{cases} \tag{9}$$

A threshold value for the averaged SED range $\Delta\overline{W}_{1,th} = 0.0633$ Nmm/mm^3 can be easily assessed by entering the threshold NSIF obtained from the cyclic R-curve analysis $\Delta K_{1,th}^V = 32.8$ MPa·m$^{0.326}$ (Fig. 6)

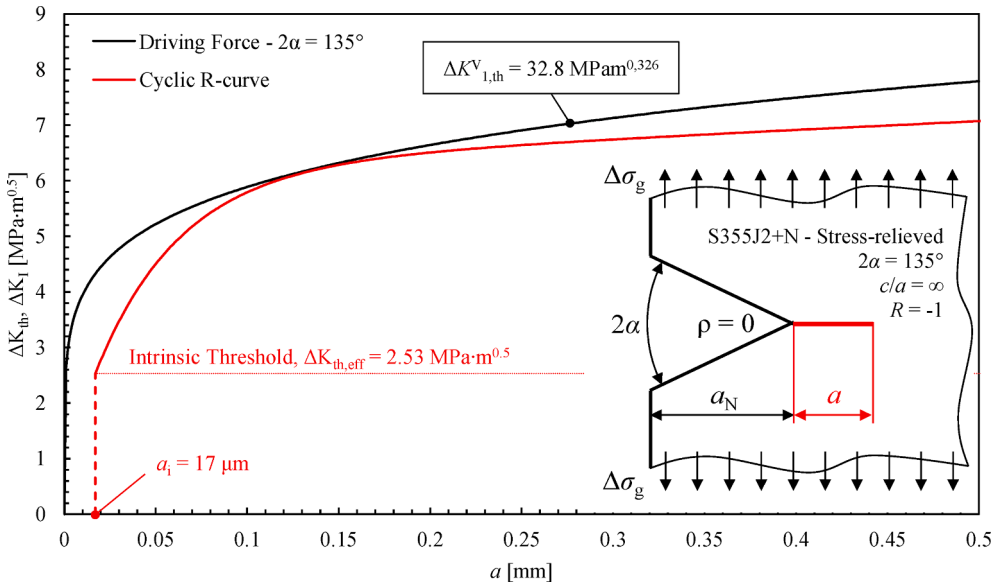

Fig. 6. The cyclic R-curve analysis: driving force of a through-the-thickness straight-fronted crack propagating along the bisector line of a sharp V-notch (ρ = 0) having opening angle 2α = 135° under fully reversed (*R* = -1) axial loading.

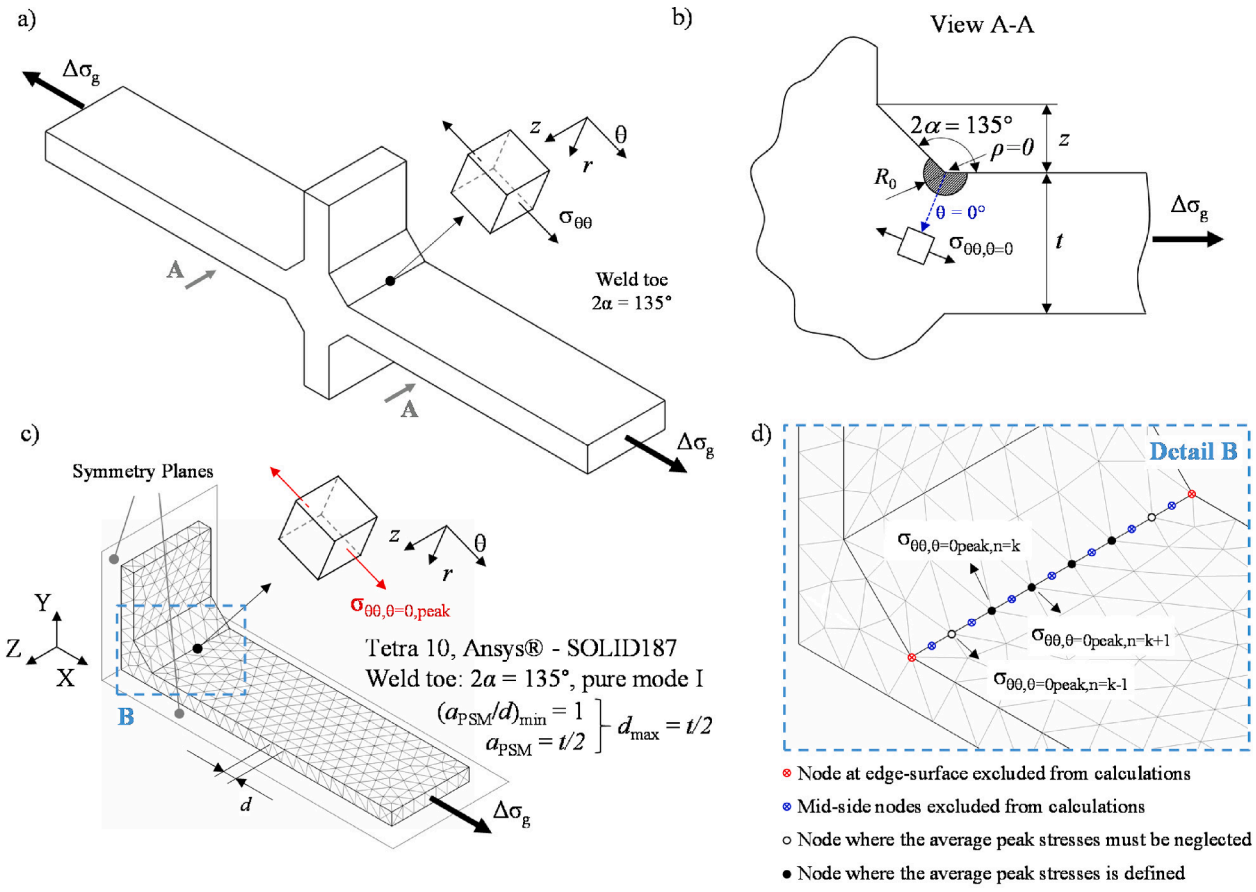

Fig. 7. The PSM applied to a full penetration cruciform joint: a) geometry according to the NSIF-based approach. b) Material-dependent structural volume having radius R_0 centred at the weld toe according to the averaged SED criterion. c) FE model discretized with 10-node tetrahedral finite elements and peak stress at the weld toe. d) guidelines to apply the PSM with 10-node tetrahedral finite elements.

into Eq. (8) with $c_{w1} = 0.5$ for $R = -1$. Then, $\Delta\overline{W}_{1,th}$ has been inserted in the SED-based fatigue design scatter band for steel welded joints proposed by Lazzarin et al. [66]. This SED-based design curve has an endurable averaged SED range $\Delta\overline{W}_{1,A,50\%} = 0.105$ Nmm/mm^3 at $N_A = 2{\cdot}10^6$ cycles, an inverse slope $k = 1.5$ and a scatter index referred to survival probabilities of 2.3%-97.7%, i.e. the mean value ± two standard deviations, $T_{\Delta\overline{W}} = 3.3$ (Fig. 8a). Moreover, as shown in Fig. 8a, $\Delta\overline{W}_{1,th} = 0.0633$ Nmm/mm^3 returns a number of cycles to failure $N_{th} \approx$

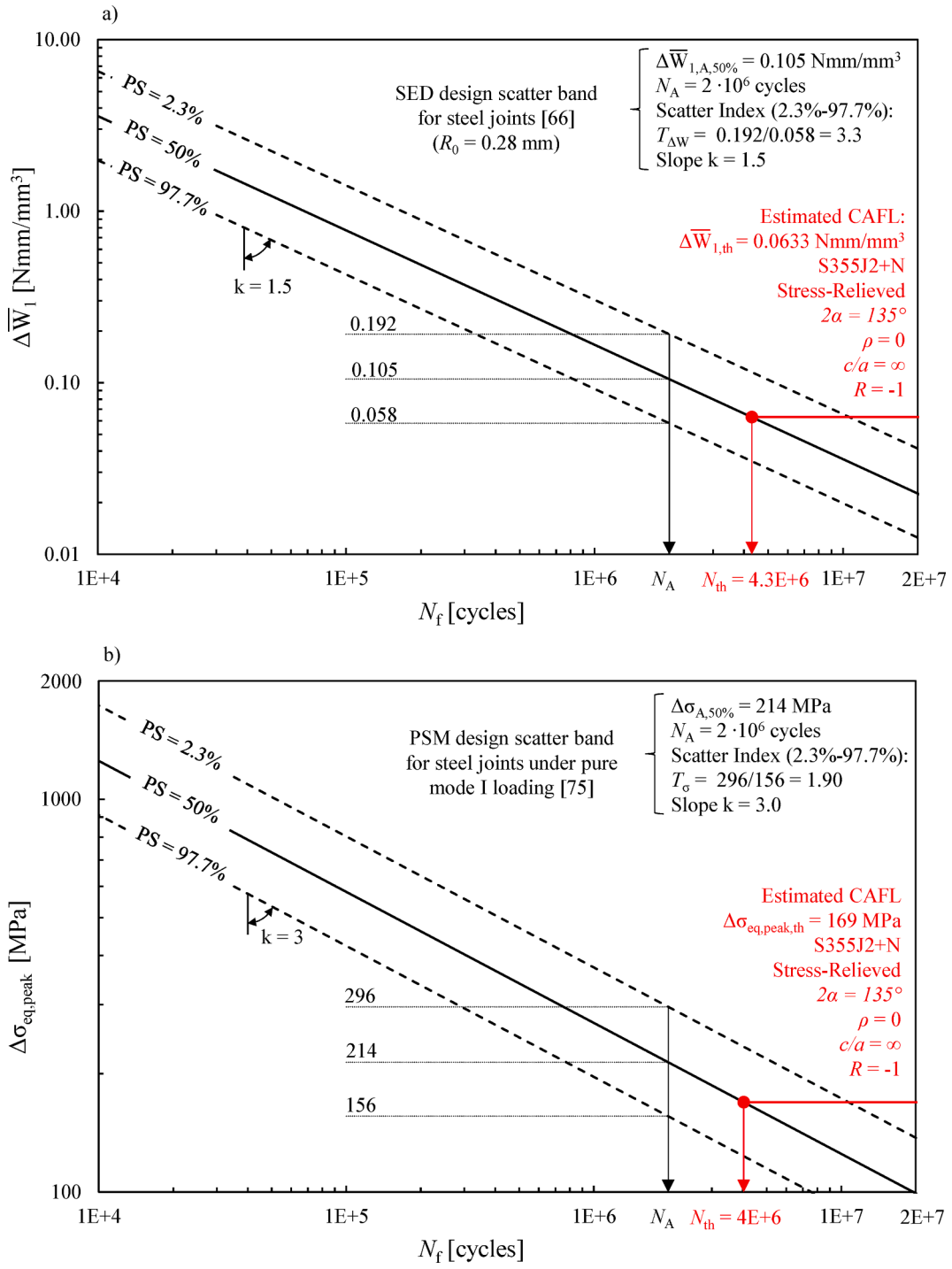

Fig. 8. a) SED-based [66] and b) PSM-based [75] design scatter bands with the Constant Amplitude Fatigue Limit (CAFL) relevant to weld toe failure of stress relieved welded joints made of S355 structural steel and tested under fully reversed loading.

$4.3{\cdot}10^6$ cycles, in good agreement with the knee point proposed by the Eurocode3 ($5{\cdot}10^6$ cycles) [1].

Unfortunately, the effectiveness of the NSIF-based approaches presented above is still limited in industrial applications, the main reason being the way NSIFs are evaluated. Indeed, Finite Element Analyses (FEA) are the easiest and effective way to compute the NSIF in complex geometries, despite analytical solutions are available in the literature for some limited cases (e.g. [67–70]). Such FEA allow to compute the NSIF by evaluating first the relevant stress distribution in the vicinity of the V-notch tip along the bisector line ($\theta = 0$ in Fig. 5) and afterwards by performing the limit calculation of Eq. (5). However, the finite element size to adopt must be very small (on the order of 10^{-4} mm [49]), an extremely dense mesh pattern being required to capture the gradient of the local stress field in the vicinity of the V-notch tip. A first solution to this problem is the so-called direct approach [71], which directly calculates the SED value $\Delta\overline{W}_1$ (Eq. (8)), inside the material structural volume having radius $R_0 = 0.28$ mm, which can be discretized with finite elements having size equal to the control radius R_0 itself; however, this value may be still small compared to the dimension of the component or structure under analysis. Another method is the "volume free", where modelling the material structural volume is unnecessary [72–74], but a more refined FE mesh pattern is necessary, the proper finite element size

to adopt being a fraction of the control radius R_0.

On the other hand, these limitations can be definitely overcome by the so-called Peak Stress Method (PSM) [33], which is a simplified engineering approach to rapidly estimate the NSIFs using linear elastic FE analyses having rather coarse FE meshes compared to that required for applying the NSIFs' definition (Eq. (5)). According to the PSM, the NSIF is estimated as follows:

$$K_1^V \cong K_{FE}^{*} \cdot \sigma_{\theta\theta,\theta=0,peak} \cdot d^{1-\lambda_1} \tag{10}$$

where K_{FE}* is a calibrated non-dimensional coefficient and d is the average size of the finite elements (Fig. 7c). Concerning $\sigma_{\theta\theta,\theta=0,peak}$, it is the nodal value of the opening (mode I) peak stress evaluated in a local cylindrical coordinate system centred at the V-notch tip, having z-direction tangent to the notch tip line, $\theta = 0$ direction aligned with the notch bisector line, and r-coordinate along the radial direction. In particular, $\sigma_{\theta\theta,\theta=0,peak}$ is the opening stress acting normal to the notch bisector line (identified by the direction $\theta = 0°$, Fig. 7c).

Taking advantage of the PSM, Meneghetti and Lazzarin [75] suggested to accelerate the SED evaluation (Eq. (8)) by using Eq. (10) and proposed a fatigue damage parameter called equivalent peak stress $\Delta\sigma_{eq,peak}$ [33,34], which was defined by equating the local SED of Eq. (8) to an equivalent uniaxial plane strain state according to the following expression:

$$\Delta\sigma_{eq,peak} = \sqrt{\frac{2E}{1-\nu^2} \cdot \Delta\bar{W}_1} \tag{11}$$

Thereafter, a PSM-based fatigue design scatter band has been defined for steel welded joints relevant to uniaxial loading [75]. The effectiveness of the equivalent peak stress range $\Delta\sigma_{eq,peak}$ to correlate the fatigue strength of welded joints have been extensively validated in previous investigations [33,34,76,77].

A threshold value of the equivalent peak stress $\Delta\sigma_{eq,peak,th} = 169$ MPa has been found by entering the averaged SED range $\Delta\overline{W}_{1,th} = 0.0633$ Nmm/mm^3 into Eq. (11). The obtained value refers to a survival probability PS = 50% and is valid for weld toe failure ($2\alpha = 135°$) of stress-relieved welded joints made of S355 structural steel under pure mode I fully reversed (R = -1) cyclic loading, according to the hypotheses aforementioned. Finally, such CAFL $\Delta\sigma_{eq,peak,th}$ has been inserted in the PSM-based fatigue design scatter band which has an endurable stress range $\Delta\sigma_{eq,peak,A,50\%} = 214$ MPa at $N_A = 2{\cdot}10^6$ cycles, an inverse slope $k = 3$ and a scatter index referred to survival probabilities of 2.3%-97.7%, i.e. the mean value ± two standard deviations, $T_\sigma = 1.90$ [75] (Fig. 8b). As shown in Fig. 8b, the obtained $\Delta\sigma_{eq,peak,th} = 169$ MPa returns a number of cycles to failure $N_{th} \approx 4{\cdot}10^6$ cycles, again in good agreement with the knee point suggested by the Eurocode3 ($5{\cdot}10^6$ cycles) [1].

2.4. FE-based evaluation of the equivalent peak stress range $\Delta\sigma_{eq,peak}$

While the previous paragraph illustrated the PSM from the material's resistance side, the present section describes the load side of the method, that is the FE analysis to evaluate the applied equivalent peak stress range $\Delta\sigma_{eq,peak}$ to use with the PSM-based fatigue design curves (Fig. 8b) to assess the fatigue strength of the investigated joint. Before going into details, it is worth mentioning that the present paper only addresses the case of pure mode I loading; however the PSM has been defined and successfully adopted also for multiaxial local stresses [34]. Moreover, for the sake of brevity, in what follows the theoretical background on the PSM will be limited to the case of 3D geometries discretized using 10-node tetrahedral elements, the case being of interest for the validation that will be presented later. However, the PSM has been calibrated also for different 2D and 3D finite elements and the reader is advised to read a recent review [34] for more details regarding the method and its conditions of applicability.

Recalling Eq. (11), by substituting Eq. (8) and Eq. (10), the equivalent peak stress range $\Delta\sigma_{eq,peak}$ can be written as follows [34,75]:

$$\Delta\sigma_{eq,peak} = \sqrt{c_{w1} \cdot f_{w1}^2 \cdot \Delta\sigma_{\theta\theta,\theta=0,peak}^2} \tag{12}$$

where the coefficient f_{w1} accounts for the stress-averaging inside the material structural volume and the adopted FE size according to the PSM [34]:

$$f_{w1} = K_{FE}^{*} \cdot \sqrt{\frac{2e_1}{1-\nu^2}} \cdot \left(\frac{d}{R_0}\right)^{1-\lambda_1} \tag{13}$$

where the coefficient K_{FE}* is calibrated for 3D finite elements available in several commercial FE software packages [34,52,78,79] and depends on the V-notch opening angle 2α, the finite element type and formulation (in terms of integration scheme and stress extrapolation at FE nodes) and the FE mesh pattern generated by the FE software. For example, K_{FE}* = 1.21 ± 15% for 10-node tetrahedral elements (SOLID 187 of Ansys® element library) and opening angle $2\alpha = 135°$ (weld toe) [34,52]. As to the 3D tetrahedral finite elements, despite their high efficiency in discretizing very complex 3D geometries, they lead to irregular FE mesh patterns along the V-notch tip line, since the FE nodes located on it share a different number of tetrahedral finite elements. The irregularity of the FE mesh pattern causes a scattered distribution of the peak stress $\sigma_{\theta\theta,\theta=0,peak}$ even in the case of 3D geometries having rigorously constant NSIFs along the V-notch tip line, which is not the case according to Eq. (10) applied to regular FE mesh patterns [80]. To smooth the peak stress distribution calculated with 10-node tetrahedral elements, the peak stress $\sigma_{\theta\theta,\theta=0,peak}$ appearing in Eq. (10) has been substituted with the corresponding average peak stress $\bar{\sigma}_{\theta\theta,\theta=0,peak}$, calculated as follows [80]:

$$\bar{\sigma}_{\theta\theta,\theta=0,peak,n=k} = \left.\frac{\sigma_{\theta\theta,\theta=0,peak,n=k-1} + \sigma_{\theta\theta,\theta=0,peak,n=k} + \sigma_{\theta\theta,\theta=0,peak,n=k+1}}{3}\right|_{n=node} \tag{14}$$

Accordingly, the average peak stress $\bar{\sigma}_{\theta\theta,\theta=0,peak}$ is defined as the moving average of the peak stresses calculated on three adjacent vertex nodes and Eq. (14) gives the example for calculating the peak stress at FE node n = k (Fig. 7d) Moreover, the peak stresses $\sigma_{\theta\theta,\theta=0,peak}$ obtained from FE nodes lying on an edge surface (red nodes in Fig. 7d) must be neglected, their values being affected by the distorted FE mesh pattern originating from those FE nodes [79,81]. Therefore, the first two FE nodes nearest to the edge surface of the structure (red nodes and empty black nodes in Fig. 7d) cannot be the target FE nodes where to compute the average peak stress $\bar{\sigma}_{\theta\theta,\theta=0,peak,n=k}$ (Eq. (14)). An additional rule is that only the vertex nodes must be considered in Eq. (14), while the mid-side FE nodes are neglected (blue nodes in Fig. 7d).

Finally, it is important to highlight that the global finite element size d to input in the free mesh generation algorithm of the FE software can be arbitrarily chosen, provided a certain mesh density ratio a_{PSM}/d is satisfied, where a_{PSM} is a reference geometrical dimension of the welded joint. The guidelines for selecting a_{PSM} and the minimum a_{PSM} $/d$ to adopt in FE analyses are reported elsewhere [34]. For example, $a_{PSM}/d \geq 1$ is required by the PSM to evaluated the peak stress at the weld toe ($2\alpha = 135°$) under pure mode 1 loading using 10-node tetrahedral finite elements, a_{PSM} being half the plate thickness t in the case of the joint with double attachments reported in Fig. 7.

The rapidity and effectiveness of PSM in the pre-processing, solving and post-processing phases make this method advantageous for industrial applications. In addition, some recent developments of the PSM like its extension to variable amplitude multiaxial loading conditions [76,77] and its automated implementation [56,57] are making the application of the PSM wider, easier and faster.

3. Validation with experimental data taken from the literature

3.1. Sonsino et al. [82]

Sonsino et al. [82] tested two series of fillet-welded double longitudinal stiffeners having different main plate thicknesses ($t = 12$ mm for series 1.1 and $t = 20$ mm for series 1.2, see Fig. 9) and made of St 52–3 (previous nomenclature by DIN17100:1980 [83] of the S355J2 EN10025-2 [84]). All specimens were tested in the stress-relieved condition under fully reversed ($R = -1$) pure axial loading and the authors reported that fatigue crack initiation always occurred at the weld toe of the main plate (Fig. 9). The recorded number of cycles N_f corresponded to complete separation of the specimen, while run-out tests were considered between $2{\cdot}10^7$ cycles and $13{\cdot}10^7$ cycles, if no failure was detected.

A 3D free FE mesh pattern of 10-node tetrahedral elements (SOLID 187 of Ansys® element library) has been defined to calculate the mode I peak stresses at the weld toe. Only one quarter of the joint geometry has been modelled by taking advantage of the YZ and ZX double symmetry. A minimum mesh density ratio $a_{PSM}/d = 1$ is necessary to analyse the weld toe ($2\alpha = 135°$) under mode I loading using 10-node tetrahedral elements according to the PSM guidelines [34], the characteristic size being $a_{PSM} = t/2$, namely d = 6 mm and d = 10 mm for series 1.1 and 1.2, respectively; therefore only one finite element on half the thickness of the main plate could be adopted (see Fig. 9). Interestingly, if the triple symmetry had been exploited and therefore one eighth of the joints had been modelled instead of one quarter, the FE node located at the crack initiation point would have been in the edge surface of the model, where the peak stress cannot be evaluated according to the PSM guidelines mentioned previously and reported in Fig. 7d. With one quarter of the joint, the symmetry boundary conditions have been applied to YZ ($u_X = 0$) and ZX ($u_Y = 0$) symmetry planes, while a uniform tensile stress of $\Delta\sigma_g = 1$ MPa has been applied to the main plate (see Fig. 9).

After solution, the maximum principal stress $\Delta\sigma_{11,peak}$ has been evaluated at the three FE nodes located along the weld toe line, by taking advantage of the approximate equivalence $\Delta\sigma_{\theta\theta,\theta=0,peak} \approx \Delta\sigma_{11,peak}$, and three values have been used in Eq. (14) to compute the average peak stress $\Delta\bar{\sigma}_{11,peak}$. Eventually, the equivalent peak stress has been calculated from Eq. (12) with $c_{w1} = 0.5$ (Eq. (9)), all data being referred to joints tested in the stress-relieved state. In more detail, the obtained values are $\Delta\sigma_{eq,peak}/\Delta\sigma_g = 1.946$ ($\Delta\sigma_{\theta\theta,\theta=0,peak}/\Delta\sigma_g = 1.647$, $f_{w1} = 1.671$) and $\Delta\sigma_{eq,peak}/\Delta\sigma_g = 2.172$ ($\Delta\sigma_{\theta\theta,\theta=0,peak}/\Delta\sigma_g = 1.555$, $f_{w1} = 1.975$) for series 1.1 and 1.2 (Fig. 9), respectively.

3.2. Hensel et al. [85]

The fatigue strength of a fillet-welded longitudinal stiffener (model 2.1 in Fig. 10) made of S355NL was investigated [85]. All specimens were tested under fully-reversed ($R = -1$) pure axial loading after stress-relieving heat treatment. Fatigue cracks always initiated at the weld toe of the main plate (Fig. 10) and the reported number of cycles N_f corresponded either to the complete specimen's separation or to the run-out condition at $1.5{\cdot}10^7$ cycles.

The mode I peak stresses at the weld toe have been calculated from a 3D FE model which has been free-meshed using 10-node tetrahedral elements and taking advantage of the YZ symmetry plane (Fig. 10). A minimum mesh density ratio $a_{PSM}/d = 1$ is required to analyse the weld toe ($2\alpha = 135°$) under mode I loading [34]. Accordingly, a FE mesh having global size $d = 12$ mm could have been used to satisfy the PSM requirements, the characteristic size being $a_{PSM} = t = 12$ mm. However, a slightly more refined mesh pattern having finite element size $d = t/2 = 6$ mm has been adopted (Fig. 10) to ensure that at least one FE node was located at the weld toe on XY plane of symmetry where the fatigue crack initiated. After solving the model, the maximum principal stress $\Delta\sigma_{11,peak}$ has been evaluated at FE nodes along the weld toe line ($\Delta\sigma_{\theta\theta,\theta=0,peak} \approx \Delta\sigma_{11,peak}$), and the average peak stress $\Delta\bar{\sigma}_{11,peak}$ (Eq. (14)) has been calculated. Then, the equivalent peak stress range has been computed with Eq. (12), by taking again $c_{w1} = 0.5$, all joints being tested under fully-reversed load in the stress-relieved state. The maximum value of the equivalent peak stress occurred where fatigue cracks experimentally initiated and was found to be $\Delta\sigma_{eq,peak}/\Delta\sigma_g = 1.831$ ($\Delta\sigma_{\theta\theta,\theta=0,peak}/\Delta\sigma_g = 1.550$, $f_{w1} = 1.671$).

3.3. Schönborn and Nitschke-Pagel [86]

Schönborn and Nitschke-Pagel [86] conducted fatigue tests on double longitudinal stiffeners with full penetration welds having main plate thicknesses $t = 12$ mm (series 3.1 in Fig. 11). The joints were made from S355NL structural steel and were tested under fully reversed axial loading under stress-relieved condition. Again, the fatigue crack

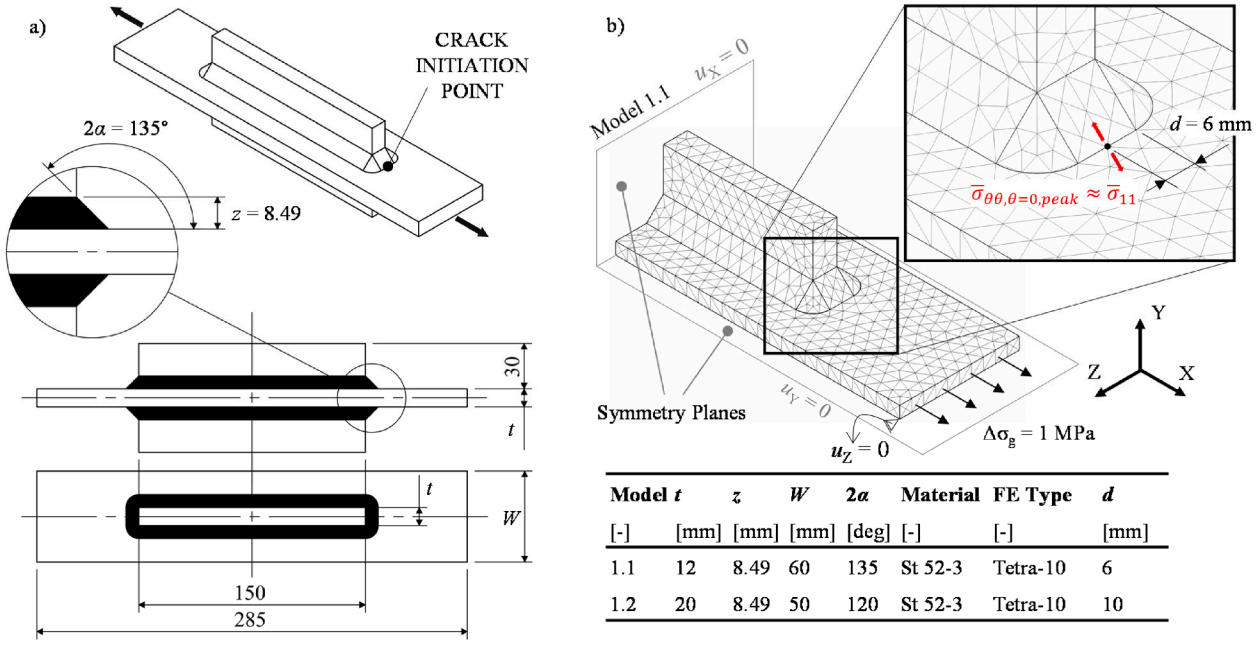

Model	t	z	W	2α	Material	FE Type	d
[-]	[mm]	[mm]	[mm]	[deg]	[-]	[-]	[mm]
1.1	12	8.49	60	135	St 52-3	Tetra-10	6
1.2	20	8.49	50	120	St 52-3	Tetra-10	10

Fig. 9. Sonsino et al. [82]: Specimens' geometry and FE model according to the PSM guidelines.

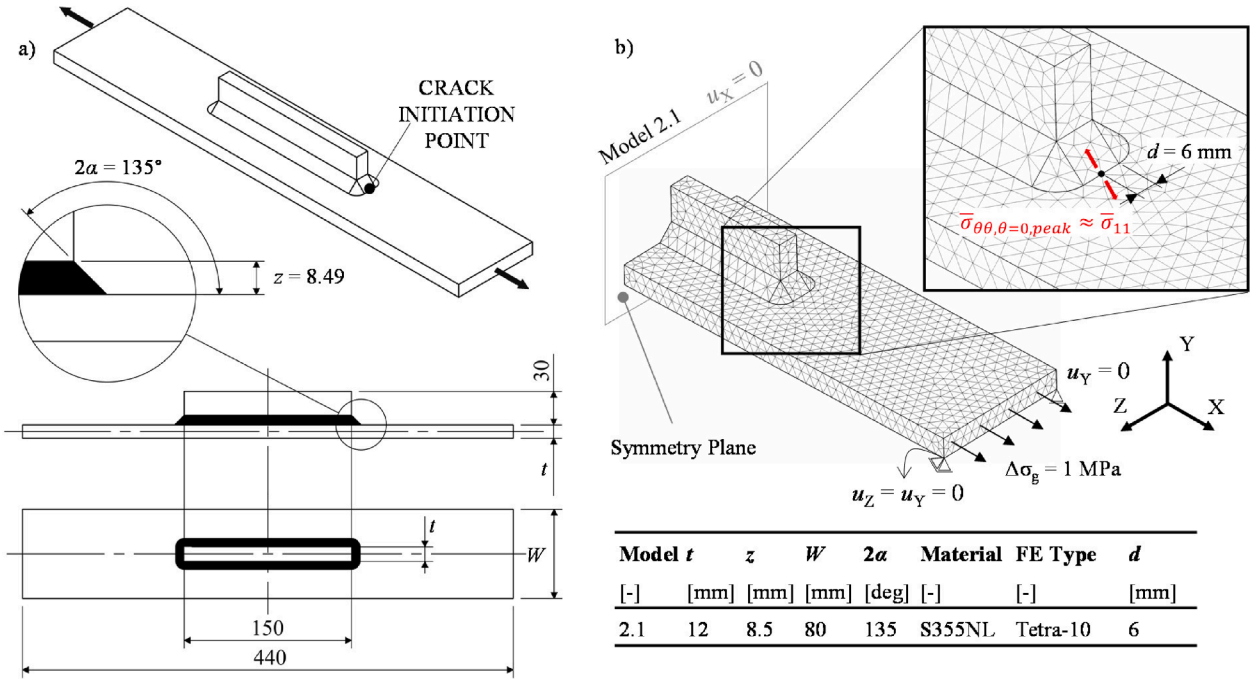

Model	t	z	W	2α	Material	FE Type	d
[-]	[mm]	[mm]	[mm]	[deg]	[-]	[-]	[mm]
2.1	12	8.5	80	135	S355NL	Tetra-10	6

Fig. 10. Hensel et al. [85]: Specimens' geometry and FE model according to the PSM guidelines.

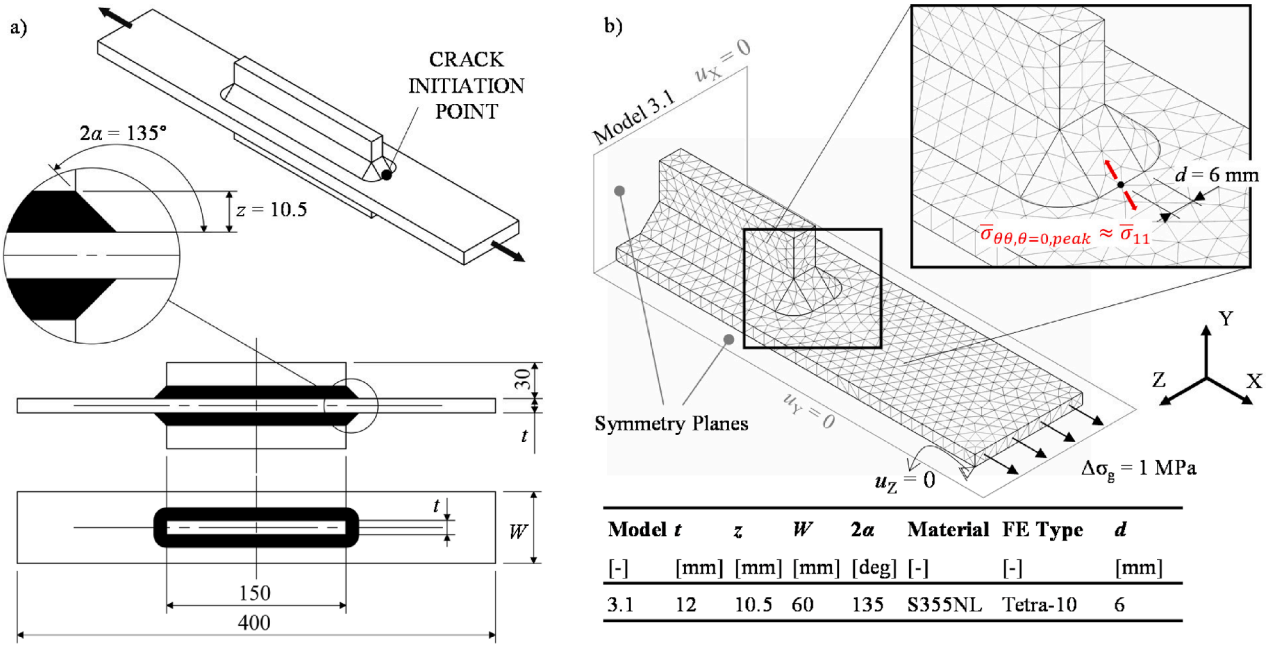

Model	t	z	W	2α	Material	FE Type	d
[-]	[mm]	[mm]	[mm]	[deg]	[-]	[-]	[mm]
3.1	12	10.5	60	135	S355NL	Tetra-10	6

Fig. 11. 3.3 Schönborn and Nitschke-Pagel [86]: Specimens' geometry and FE model according to the PSM guidelines.

initiation was found at the weld toe of the main plate. The failure criterion was defined as complete separation of the joint, while the run-out condition was fixed to 10^8 cycles.

A finite element mesh pattern of 3D 10-node tetrahedral elements was used to analyse the mode I peak stresses at the weld toe. The joint has been modelled using YZ and ZX double symmetry, covering only a quarter of the entire joint. A FE mesh having global size $d = 6$ mm has been used, the minimum mesh density ratio being $a_{PSM}/d = 1$, with a characteristic size of $a_{PSM} = t/2 = 6$ mm (Fig. 11). Finally, the symmetry boundary conditions has been applied to the model along with a uniform nominal stress of 1 MPa (Fig. 11). Thereafter, the maximum principal stress $\Delta\sigma_{11,peak}$ has been evaluated at FE nodes located at the weld toe ($\Delta\sigma_{\theta\theta,\theta=0,peak} \approx \Delta\sigma_{11,peak}$) and the corresponding average peak stress $\Delta\bar{\sigma}_{11,peak}$ has been calculated thanks to Eq. (14). Eventually, the maximum equivalent peak stress $\Delta\sigma_{eq,peak}$ was found at the crack initiation point and resulted $\Delta\sigma_{eq,peak}/\Delta\sigma_g = 1.888$ ($\Delta\sigma_{\theta\theta,\theta=0,peak}/\Delta\sigma_g = 1.598$, $f_{w1} = 1.671$, $c_{w1} = 0.5$).

3.4. Fatigue strength assessment according to the PSM

The original references [82,85,86] reported fatigue data in terms of number of cycles to failure N_f versus applied nominal stress range $\Delta\sigma_g$, the latter being evaluated with reference to the main plate according to the following expression:

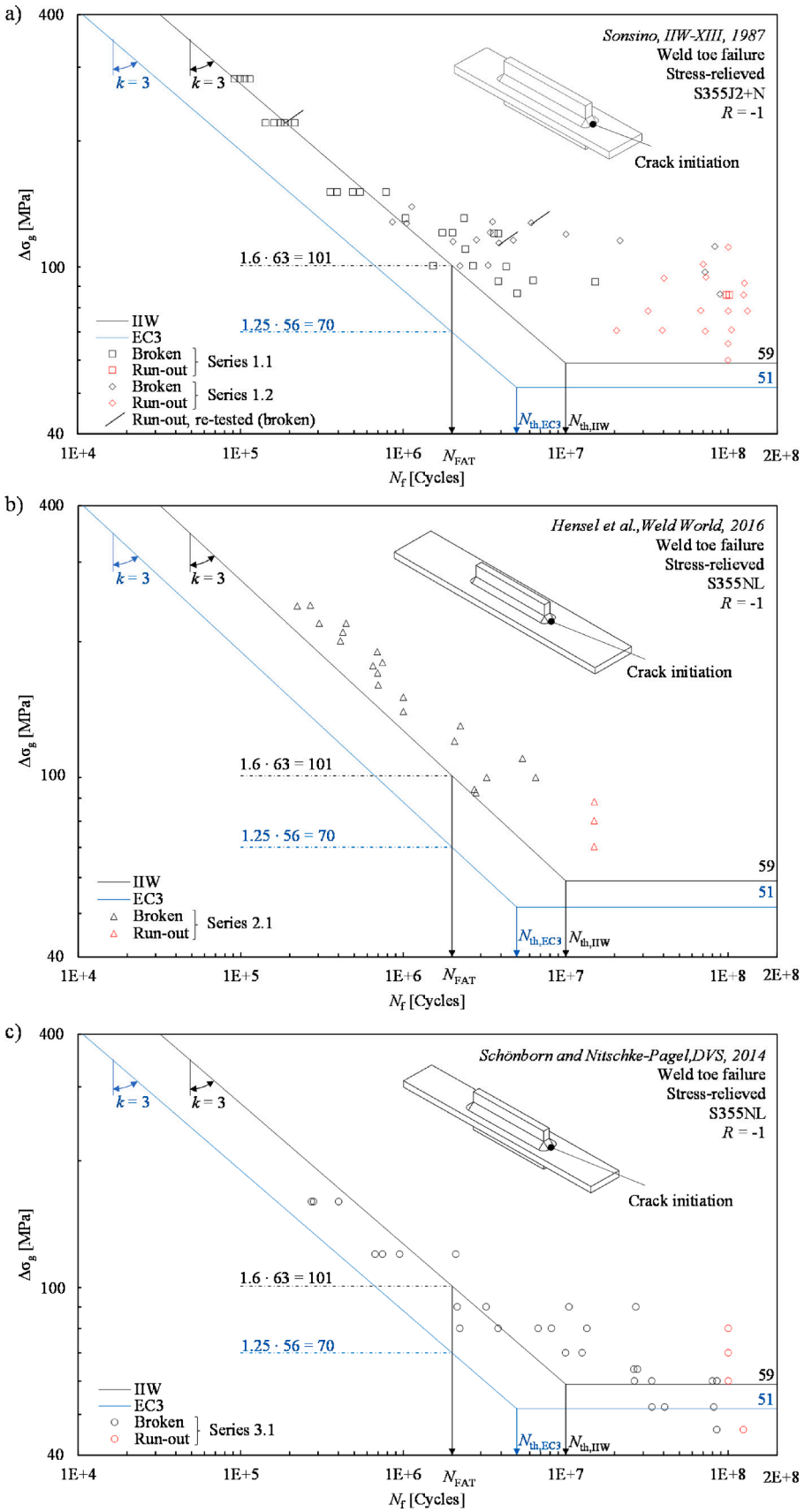

Fig. 12. Comparison between FAT classes of longitudinal stiffners according to IIW Recommendations [2], Eurocode3 [1], and experimental data from a) Sonsino et al. [82], b) Hensel et al. [85], and c) Schönborn and Nitschke-Pagel [86].

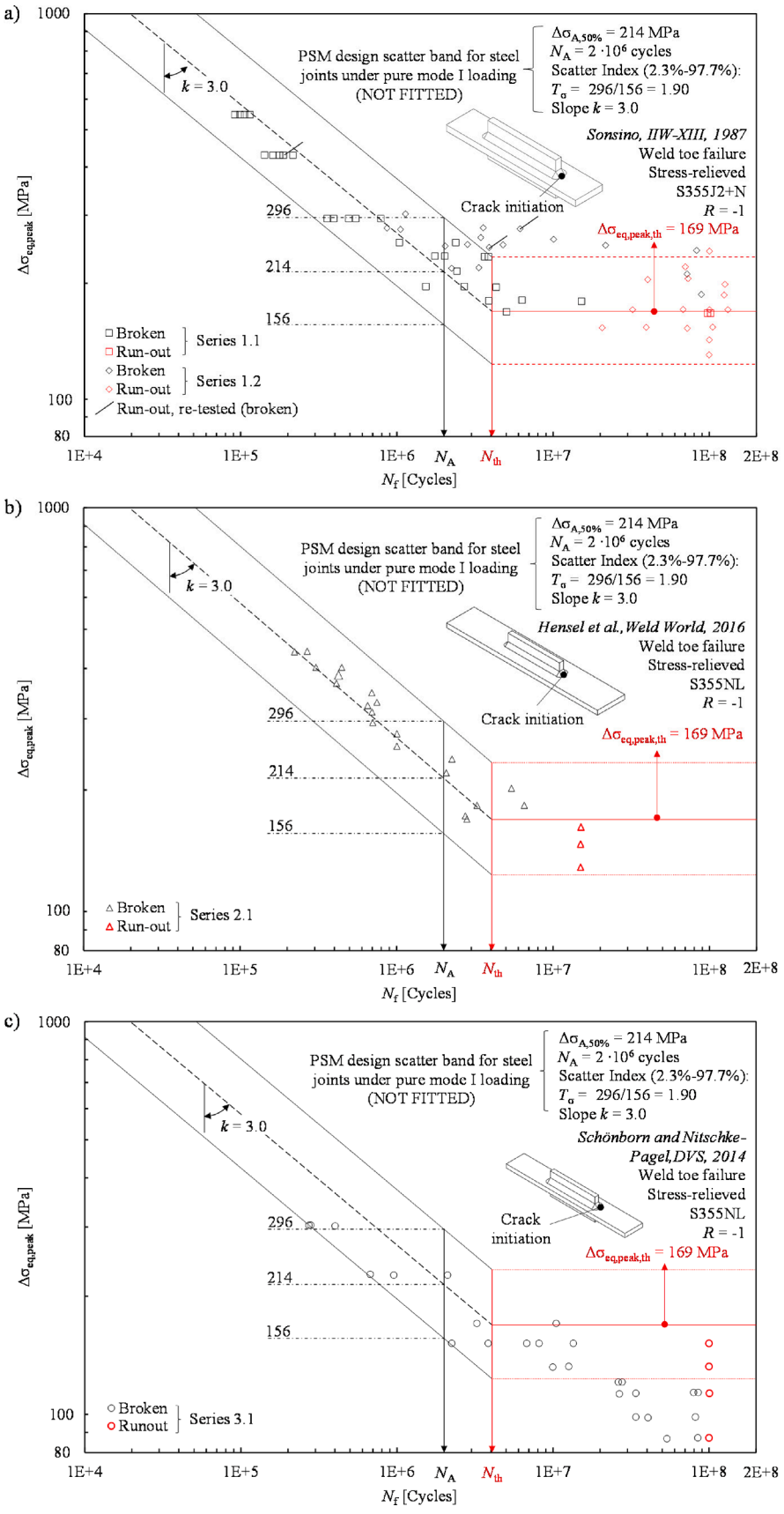

Fig. 13. Fatigue strength assessment of welded joints adopting the PSM with the CAFL: comparison between the PSM design scatter band and experimental data from a) Sonsino et al. [82], b) Hensel et al. [85], and c) Schönborn and Nitschke-Pagel [86].

$$\Delta\sigma_g = \frac{\Delta F}{A} = \frac{\Delta F}{W \cdot t} \tag{15}$$

where ΔF is the axial load range, $A = W \cdot t$ is the cross-sectional area, W being the plate width. Experimental data from [82,85,86] are shown in Fig. 12 with inclusion of the uniaxial fatigue resistance curves according to IIW Recommendations [2] and Eurocode 3 [1]. The design curve for joints having 150-mm-long longitudinal stiffners (Figs. 9-11) depends on the standard adopted and the fatigue strengths at $2{\cdot}10^6$ cycles (FAT class) are $\Delta\sigma_{FAT,IIW} = 63$ MPa and $\Delta\sigma_{FAT,EC3} = 56$ MPa for IIW Recommendations [2] and Eurocode 3 [1], respectively. The mean stress correction of the fatigue strength is also required, all specimens being tested in the stress-relieved state [1,2]. IIW [2] provides an enhancement factor $f(R)$, which depends on the level of residual stresses and on the applied load ratio R ($f(R) = 1.6$ in case of stress-relieved welded joints under fully reversed loading, R = -1); accordingly, the FAT class becomes $\Delta\sigma_{FAT,IIW} = 1.6{\cdot}63 = 101$ MPa (Fig. 12). On the other hand, Eurocode 3 [1] suggests using an effective stress range which is obtained by considering 60% of the compressive portion of the stress range, that is $\Delta\sigma_g = |\sigma_{g,max}| + 0.6{\cdot}|\sigma_{g,min}|$. In the case of R = -1, this approach corresponds to an enhancement factor on the resistance side equal to $f(R) = 2/1.6 = 1.25$, which is lower than the enhancement factor suggested by IIW. Therefore, the considered FAT class becomes $\Delta\sigma_{FAT,EC3} = 1.25{\cdot}56$ MPa = 70 MPa (Fig. 12). The corresponding Constant Amplitude Fatigue Limits are also shown in Fig. 12, their values being $\Delta\sigma_{th,IIW} = 59$ MPa at 10^7 cycles for IIW recommendations [2] and $\Delta\sigma_{th,EC3} = 51$ MPa at $5{\cdot}10^6$ cycles for Eurocode 3 [1].

Afterwards, original fatigue data (Fig. 12) have been converted from nominal stress ranges $\Delta\sigma_g$ (Eq. (15)) to equivalent peak stress ranges $\Delta\sigma_{eq,peak}$ (Eq. (12)) evaluated at the crack initiation point. Thanks to the linear elasticity assumption, the nominal stress ranges $\Delta\sigma_g$ have been multiplied by the corresponding equivalent peak stress range $\Delta\sigma_{eq,peak}/\Delta\sigma_g$ obtained from FEA with 1 MPa applied to the model (see paraghraphs 3.1, 3.2, and 3.3). Then, the fatigue data have been compared with the pre-existing PSM-based fatigue design scatter band for steel arc-welded joints under pure mode I loading [34,75] (Fig. 8b). The results are reported in Fig. 13, which shows that the PSM-based estimations are in very good agreement with experimental data in the finite-life region, because the design curve having PS = 50 % captures the average experimental trend. Concerning the infinite-life region, Fig. 13 shows that the novel threshold value for the equivalent peak stress $\Delta\sigma_{eq,peak,th} = 169$ MPa describes well the CAFL of welded joints tested by Sonsino et al. [82] (Fig. 13a) and by Hensel et al. [85] (Fig. 13b), since the $\Delta\sigma_{eq,peak,th}$ (horizontal solid red line) separates with sufficient accuracy the data points of broken specimens (black markers) from the run-out ones (red markers). Conversely, the PSM overestimates the fatigue strength of the joints tested by Schönborn and Nitschke-Pagel [86] in the infinite-life region, because the experimental data fall below the CAFL estimated with the PSM (Fig. 13c). Similarly, the nominal stress approach according both to IIW [2] and Eurocode 3 [1] overestimates the CAFL (Fig. 12c). The reasons for this inaccuracy may be due to the angular misalignments (defined as the axial angle between the specimens' ends) noted by the authors of the original paper, who reported that the measured angular misalignments were ~ 0.4° in the as-welded conditions and increased to ~ 0.8° after the stress-relieving heat treatment [86]. The investigation [85] confirms this hypothesis, in that the authors state that the reduced fatigue strength found in the study [86] can be justified by high bending stresses induced by the angular misalignments. In fact, the authors of ref [85] report that care has been taken when preparing their specimens to avoid unpredictable and detrimental secondary bending stresses. In particular, the authors proposed a procedure to straighten the specimens and reduce their angular misalignment from >1.0° to values ranging from 0.09° and 0.15° [85]. Eventually, the same authors [85] performed strain gauge measurements to evaluate the deformations induced by clamping in the test machine both before and after the mitigation of the angular misalignments. Interestingly, they observed that the secondary bending strains was reduced by a factor of 5 after reducing the angular misalignments, resulting in almost negligible effects on the applied stress [85]. Unfortunately, no considerations about angular misalignments are possible for joints tested by Sonsino et al. [82], since the authors did not report any value of misalignments or secondary bending stresses.

4. Discussion

4.1. Effect of the initial crack size a_i

An initial crack size a_i = 17 μm has been adopted in the present investigation (Fig. 6), according to the crack arrest analysis relevant to a

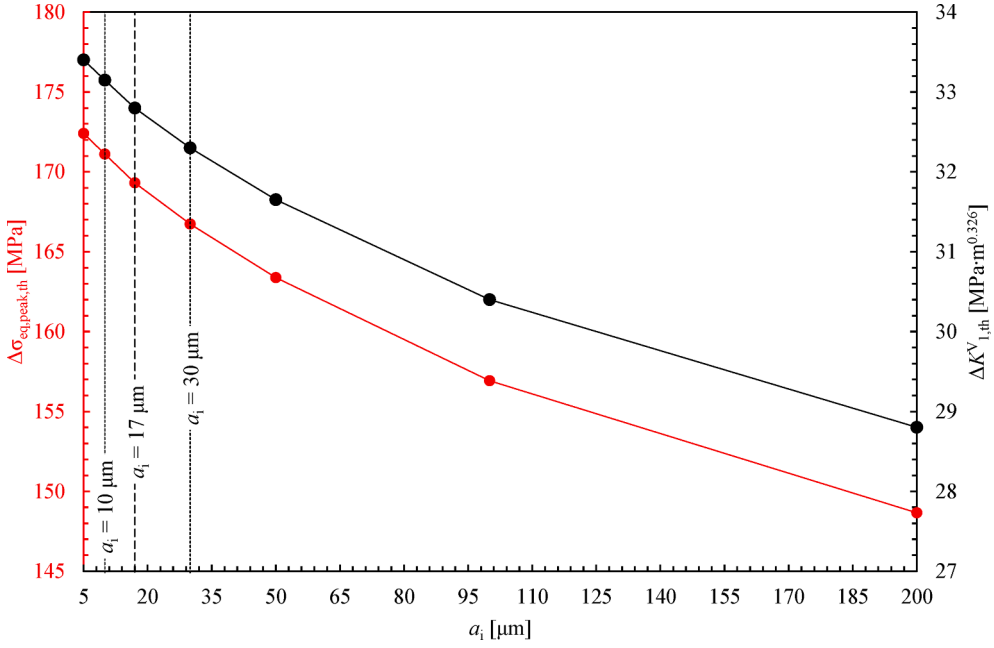

Fig. 14. Dependency of the threshold NSIF $\Delta K^V_{1,th}$ and the equivalent peak stress $\Delta\sigma_{eq,peak,th}$ on the initial through-the-thickness straight-fronted crack size a_i (see Fig. 6).

S355NL structural steel [45]. The initial crack size a_i is obtained by shifting the cyclic R-curve $\Delta K_{th}(a)$ along the abscissa until the tangency condition with the driving force is achieved, where the latter is evaluated at a stress level equal to the plain material fatigue limit $\Delta K_{I,\Delta\sigma 0}(a)$ [26,29,30,45]. However, the initial crack size can be defined by means of other criteria, which take into consideration [26]:

- The grain size [87,88].
- The size of the fatigue process zone [89,90].
- An intrinsic crack length [91].
- The size of the cyclic plastic zone [92].

An accurate comparison between all cited methods has been carried out by Zerbst et al. [26], who considered the case of a S355NL structural steel. Interestingly, the authors observed that all criteria result in almost the same initial crack size a_i, which was found in the range from 10 to 30 μm for a S355 steel. Accordingly, the cyclic R-curve analysis discussed in paragraph 2.2 and reported in Fig. 6 has been repeated assuming different values of initial crack size a_i from 5 to 200 μm. The results are reported in Fig. 14, where the threshold values of the NSIF $\Delta K^V_{1,th}$ and the equivalent peak stress $\Delta\sigma_{eq,peak,th}$ are reported as a function of a_i. Interestingly, Fig. 14 highlights that the variability of a_i reported in the literature for a S355 steel (10 μm $\leq a_i \leq$ 30 μm) causes little variations of the thresholds $\Delta K^V_{1,th}$ and $\Delta\sigma_{eq,peak,th}$, which are always smaller than ± 2%. It is worth noting that imposing a very high value a_i = 200 μm, which is one order of magnitude greater than a_i = 17 μm, the threshold values are reduced only by approximately 12%.

4.2. Effects of the crack path and the crack shape c/a

Evaluating the driving force requires some assumptions concerning the location, path and shape of the propagating crack, which are discussed in this section.

While the crack initiation point could be easily identified with the sharp V-notch tip, i.e. the weld toe, Eq. (6) assumes the fatigue crack path is aligned with the notch bisector line, this being justified by experimental observations made by Livieri and Tovo [56]. In more detail, they analysed many welded joint geometries (flange–tube-connections, butt-welded joints, cruciform joints) subjected to pure mode I loading and observed that fatigue cracks initiated at the weld toes propagate along the bisector line in the first stage and subsequently the crack path progressively deviates to become perpendicular to the load direction [56].

As to the crack shape, usually semi-elliptical fatigue cracks are assumed to propagate from the weld toe line, characterized by crack depth a and aspect ratio c/a (Fig. 15). Although a semi-circular crack $c/a = 1$ is commonly assumed in the literature (at least at the initiation stage) [2,29,30,45], several studies have found higher aspect ratios $c/a > 1$ [29,93–104]. Maddox [100,104] investigated the crack shape on fillet-welded longitudinal stiffeners made of BS 968:1962 steel with main plate thickness of 12.7 mm. A relatively high aspect ratios c/a was found in the short crack regime (Fig. 15) with an approximate linear relationship existing between a and $2c$, which was written as follows:

$$\frac{c}{a} = 1.290 + \frac{3.355}{a^{[mm]}} \tag{16}$$

Eq. (16) suggests that the smaller the crack size a the higher the aspect ratio c/a, i.e. short cracks at the weld toe are practically straight-fronted. Interestingly, this outcome is in very good agreement with Verreman et al. [105,106], who found a similar behaviour on a different joint geometry. According to Verreman et al. [105,106], the reason for such a straight-fronted crack shape at early stage of crack propagation is the intense stress concentration effect at the weld toe, which promotes the propagation along the weld toe line, while slows down propagation through the plate thickness, since stresses suddenly decrease beneath the surface. A further explanation has been provided by Schork et al. [101] and Madia et al. [29], who reported that the very high aspect ratio c/a has to be attributed to the coalescence of adjacent small cracks at the weld toe. The number of propagating small cracks and therefore the development of c/a depends on the applied stress range.

FE simulations have been carried out to further investigate the effect of the aspect ratio c/a on the driving force. In particular, the fillet-welded longitudinal stiffeners fatigue tested by Sonsino et al. [82] (see series 1.1 in Fig. 9) have been considered. Half the specimen's geometry has been modelled in Ansys Workbench environment by exploiting the YZ symmetry plane (Fig. 16). Next, a semi-elliptical crack has been

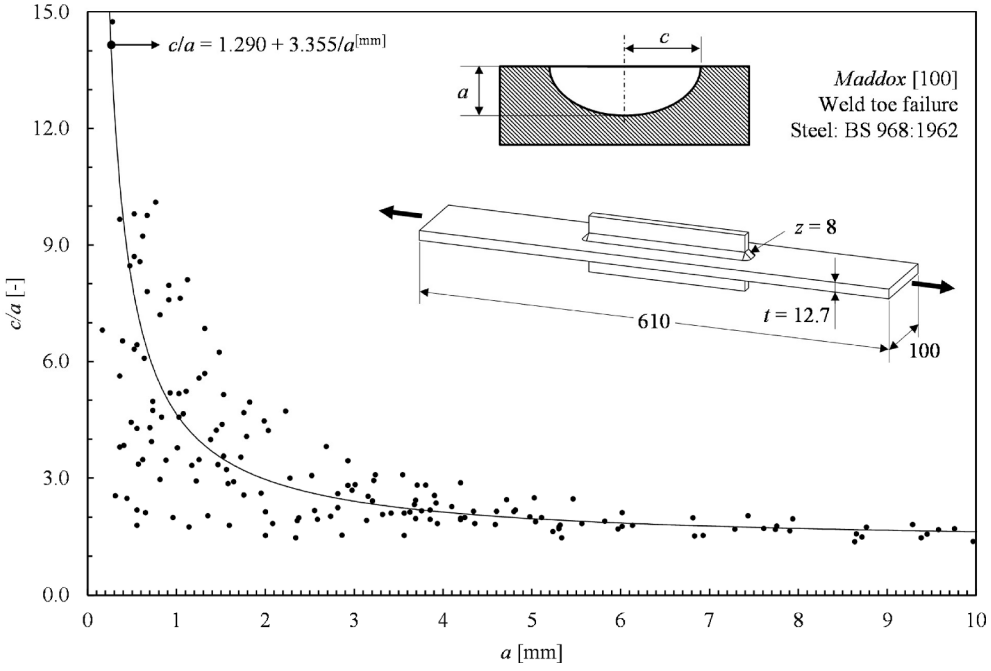

Fig. 15. Variation of the crack front shape c/a during fatigue tests of fillet-welded double longitudinal stiffeners. Re-. adapted from [100]

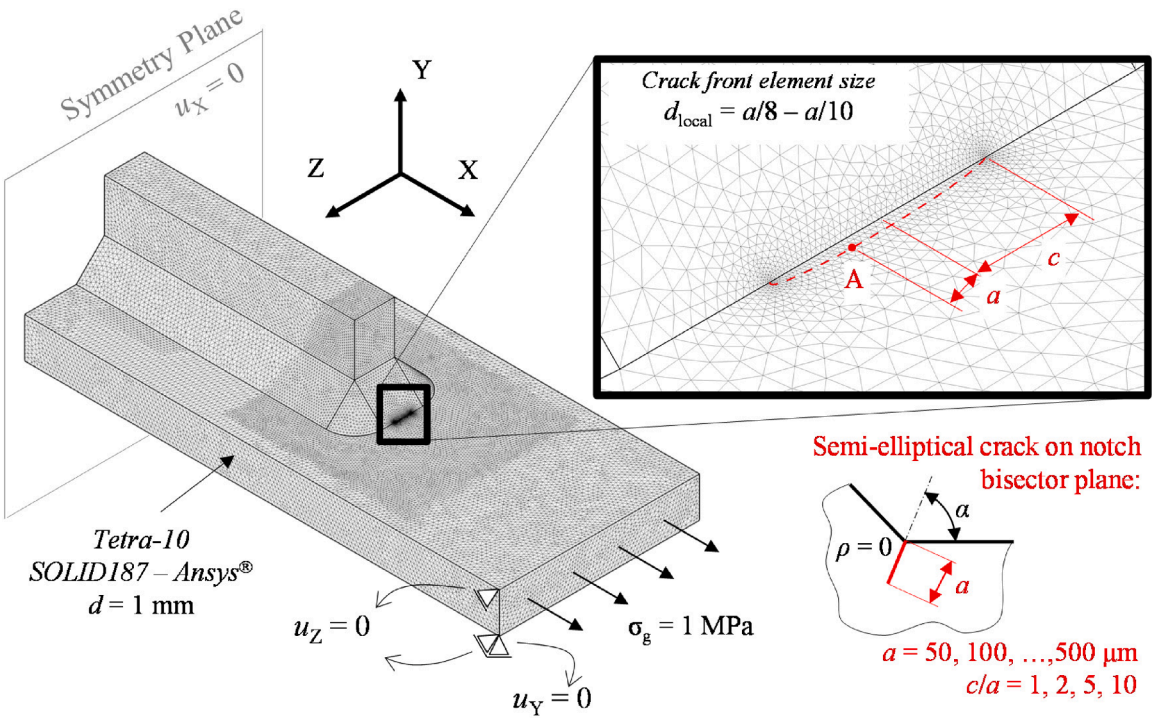

Fig. 16. FE model for investigating the effect of the crack shape on the applied SIF in the specimen's geometry 1.1 of Fig. 9 (Sonsino et al. [82]).

modelled on the bisector plane of the weld toe line, where the crack was centred symmetrically to the XY plane. According to Fig. 16 the crack depth a lies on the bisector plane and the crack width $2c$ lies on the weld toe line. The hypothesis of symmetry on the YZ plane was assumed to be still valid due to the small crack sizes involved in the analysis, which ranged from 50 μm to 500 μm stepped by 50 μm; the aspect ratios have been kept constant and equal to c/a = 1, 2, 3, 5, and 10 during the propagation. Moreover, the same crack's depths have been investigated assuming the variation of aspect ratio c/a according to Eq. (16). A global finite element size $d = 1$ mm has been adopted to discretize the model by means of 10-node tetrahedral elements, while their size has been progressively reduced to $d_{local} = a/8 - a/10$ at the crack front. The symmetry boundary conditions along YZ plane have been applied to the model along with a uniform nominal stress of 1 MPa (Fig. 16). The applied SIF has been evaluated at the deepest point of the crack (point A in Fig. 16) by using the Fracture Tool implemented in Ansys® Workbench, which exploits the domain integral method [107,108] to evaluate the SIF.

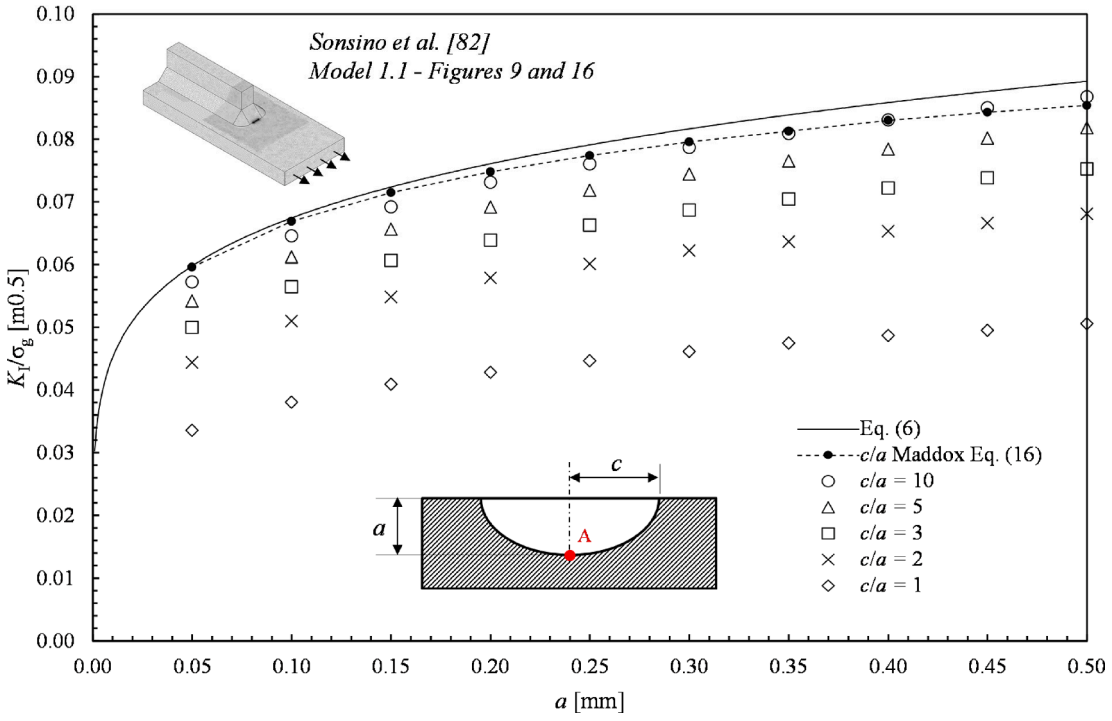

Fig. 17. Effect of the crack shape c/a on the driving force.

The results obtained are reported in Fig. 17, wherein the normalised SIF K_I/σ_g, is shown versus the crack length a. Fig. 17 also shows the driving force according to Eq. (6) (solid black line in Fig. 17) where the NSIF K_1^V has been calculated by using the peak stress of paragraph 3.1 into Eq. (10) ($K_1^V = K_{FE}{}^* \cdot \sigma_{\theta\theta,\theta=0,peak} \cdot d^{1-\lambda 1} = 1.21 \cdot 1.647 \cdot 6^{0.326} = 3.574$ MPa·mm$^{0.326}$). It can be seen that an increase of the aspect ratio c/a translates into an increase of the applied SIF K_I at point A, the highest driving force being relevant to a through-the-thickness straight-fronted crack ($c/a = \infty$, solid line in Fig. 17). The results also show that within the range of investigated crack sizes no significant differences can be found between $c/a = \infty$ (solid line in Fig. 17) and c/a equal to 5 or 10 (triangular and circular markers in Fig. 17), the errors being always smaller than 7–10% or 2–5%, respectively. A very good agreement exists also between Eq. (6) (solid line in Fig. 17) and Eq. (16) (dashed line in Fig. 17). Consequently, it can be concluded that the simplifying assumption of a through-the-thickness straight-fronted crack provides a sufficiently accurate description of the experimental driving force for the longitudinal stiffeners analysed in the present investigation.

5. Conclusions

The Peak Stress Method (PSM) has been extended to include the Constant Amplitude Fatigue Limit (CAFL) in the fatigue design curve. The simplifying hypothesis of a through-the-thickness straight-fronted crack emanating from a sharp V-notch tip has been adopted to evaluate the range of the Notch Stress Intensity Factor (NSIF) at threshold, according to the crack arrest analysis of the R-curve method. To apply this model, the V-notch opening angle has been taken to be 135°, which is appropriate for weld toes, and the R-curve of the material has been determined in the heat affected zone (HAZ) by means of dedicated experimental tests. The threshold range of the Notch Stress Intensity factor has been readily converted to the corresponding threshold range of the equivalent peak stress and incorporated in the fatigue design curve of the PSM. Eventually, the PSM with inclusion of the CAFL has been successfully validated against experimental data taken from the literature and relevant to stress-relieved longitudinal stiffeners subjected to push–pull uniaxial loading. Within the conditions of applicability highlighted in the present investigation, the advantage of the proposed method is that time-consuming stress analyses to calculate the driving force as a function of the crack length become unnecessary.

CRediT authorship contribution statement

Luca Vecchiato: Methodology, Formal analysis, Investigation, Validation, Writing – original draft. **Mauro Madia:** Methodology, Writing – review & editing. **Giovanni Meneghetti:** Conceptualization, Methodology, Validation, Writing – review & editing, Supervision.

Declaration of Competing Interest

The authors declare that they have no known competing financial interests or personal relationships that could have appeared to influence the work reported in this paper.

Data availability

Data will be made available on request.

References

[1] EN. Eurocode 3: Design of steel structures – part 1–9: Fatigue 2005.
[2] A.F. Hobbacher, Recommendations for Fatigue Design of Welded Joints and Components, in: International Institute of Welding - IIW Collection, Springer International Publishing, 2016, https://doi.org/10.1007/978-3-319-23757-2.
[3] D. Radaj, C.M. Sonsino, W. Fricke, Fatigue assessment of welded joints by local approaches, 2nd ed., Woodhead Publishing, Cambridge, England, 2006.
[4] Radaj D, Vormwald M. Advanced Methods of Fatigue Assessment. 1st ed. Berlin: Springer Berlin Heidelberg; 2013. 10.1007/978-3-642-30740-9.
[5] A.J. Fenner, N.B. Owen, C.E. Phillips, A Note on the Fatigue Crack regarded as a Stress Raiser, Engineering 171 (1951) 637.
[6] N.E. Frost, Crack Formation and Stress Concentration Effects in Direct Stress Fatigue, Engineer 200 (1955) 464–501.
[7] N.E. Frost, Non-Propagating Cracks in Vee- Notched Specimens Subject to Fatigue Loading, Aeronaut. Q. 8 (1957) 1–20, https://doi.org/10.1017/S0001925900010362.
[8] R.A. Smith, K.J. Miller, Prediction of fatigue regimes in notched components, Int. J. Mech. Sci. 20 (1978) 201–206, https://doi.org/10.1016/0020-7403(78)90082-6.
[9] K.J. Miller, The two thresholds of fatigue behaviour, Fatigue Fract. Eng. Mater. Struct. 16 (1993) 931–939, https://doi.org/10.1111/j.1460-2695.1993.tb00129.x.
[10] Y. Murakami, Metal Fatigue: Effects of Small Defects and Nonmetallic Inclusions. Second Edi, Elsevier, London, UK, 2019.
[11] T.L. Anderson, Fracture Mechanics, Fundamentals and Applications, 3rd ed., CRC Press LLC, Boca Raton, 2009.
[12] U. Zerbst, M. Vormwald, R. Pippan, H.-P. Gänser, C. Sarrazin-Baudoux, M. Madia, About the fatigue crack propagation threshold of metals as a design criterion – A review, Eng. Fract. Mech. 153 (2016) 190–243, https://doi.org/10.1016/j.engfracmech.2015.12.002.
[13] K. Minakawa, J.C. Newman, A.J. McEvily, A critical study of the crack closure effect on near-threshold fatigue crack growth, Fatigue Fract. Eng. Mater. Struct. 6 (1983) 359–365, https://doi.org/10.1111/j.1460-2695.1983.tb00351.x.
[14] A.J. McEvily, M. Endo, Y. Murakami, On the (area)^0.5 relationship and the short fatigue crack threshold, Fatigue Fract. Eng. Mater. Struct. 26 (2003) 269–278, https://doi.org/10.1046/j.1460-2695.2003.00636.x.
[15] M.D. Chapetti, J. Belmonte, T. Tagawa, T. Miyata, Integrated fracture mechanics approach to analyse fatigue behaviour of welded joints, Sci. Technol. Weld. Join. 9 (2004) 430–438, https://doi.org/10.1179/136217104225021634.
[16] W. Elber, Fatigue crack closure under cyclic tension, Eng. Fract. Mech. 2 (1970) 37–45, https://doi.org/10.1016/0013-7944(70)90028-7.
[17] R.O. Ritchie, Mechanisms of fatigue crack propagation in metals, ceramics and composites: Role of crack tip shielding, Mater. Sci. Eng. A 103 (1988) 15–28, https://doi.org/10.1016/0025-5416(88)90547-2.
[18] S. Suresh, Fatigue of Materials, Cambridge University Press, Second Edi, 2003.
[19] R.W. Hertzberg, On the calculation of closure-free fatigue crack propagation data in monolithic metal alloys, Mater. Sci. Eng. A 190 (1995) 25–32, https://doi.org/10.1016/0921-5093(94)09610-9.
[20] R. Pippan, F.O. Riemelmoser, Modeling of Fatigue Crack Growth: Dislocation Models, in: R.O. Ritchie, Y. Murakami (Eds.), Comprehensive Structural Integrity, Elsevier, 2003, pp. 191–207, https://doi.org/10.1016/B0-08-043749-4/04035-0.
[21] K. Tanaka, Y. Akiniwa, Resistance-curve method for predicting propagation threshold of short fatigue cracks at notches, Eng. Fract. Mech. 30 (1988) 863–876, https://doi.org/10.1016/0013-7944(88)90146-4.
[22] B. Tabernig, R. Pippan, Determination of the length dependence of the threshold for fatigue crack propagation, Eng. Fract. Mech. 69 (2002) 899–907, https://doi.org/10.1016/S0013-7944(01)00129-1.
[23] M. Endo, A.J. McEvily, Prediction of the behavior of small fatigue cracks, Mater. Sci. Eng. A 468–470 (2007) 51–58, https://doi.org/10.1016/j.msea.2006.09.084.
[24] J. Maierhofer, S. Kolitsch, R. Pippan, H.-P. Gänser, M. Madia, U. Zerbst, The cyclic R-curve – Determination, problems, limitations and application, Eng. Fract. Mech. 198 (2018) 45–64, https://doi.org/10.1016/j.engfracmech.2017.09.032.
[25] A. Pourheidar, L. Patriarca, M. Madia, T. Werner, S. Beretta, Progress in the measurement of the cyclic R-curve and its application to fatigue assessment, Eng. Fract. Mech. 260 (2022), 108122, https://doi.org/10.1016/j.engfracmech.2021.108122.
[26] U. Zerbst, M. Madia, M. Vormwald, Applying fracture mechanics to fatigue strength determination – Some basic considerations, Int. J. Fatigue 126 (2019) 188–201, https://doi.org/10.1016/j.ijfatigue.2019.05.009.
[27] Y. Akiniwa, L.M. Zhang, K. Tanaka, Prediction of the fatigue limit of cracked specimens based on the cyclic R-curve method, Fatigue Fract. Eng. Mater. Struct. 20 (1997) 1387–1398, https://doi.org/10.1111/j.1460-2695.1997.tb01497.x.
[28] A. Pourheidar, D. Regazzi, S. Cervello, S. Foletti, S. Beretta, Fretting fatigue analysis of full-scale railway axles in presence of artificial micro-notches, Tribol. Int. 150 (2020), 106383, https://doi.org/10.1016/j.triboint.2020.106383.
[29] Madia M, Zerbst U, Th. Beier H, Schork B. The IBESS model – Elements, realisation and validation. Eng Fract Mech 2018;198:171–208. 10.1016/j.engfracmech.2017.08.033.
[30] Zerbst U, Madia M, Schork B, Hensel J, Kucharczyk P, Ngoula D, et al. Fatigue and Fracture of Weldments: The IBESS Approach for the Determination of the Fatigue Life and Strength of Weldments by Fracture Mechanics Analysis. Cham: Springer International Publishing; 2019. 10.1007/978-3-030-04073-4_1.
[31] Murakami Y. Stress intensity factors handbook. vol. 1–2. Japan: 1987.
[32] Tada H, Paris PC, Irwin GR. The stress analysis of cracks handbook. Third Edit. New York: ASME Press; 2000.
[33] G. Meneghetti, P. Lazzarin, Significance of the elastic peak stress evaluated by FE analyses at the point of singularity of sharp V-notched components, Fatigue Fract. Eng. Mater. Struct. 30 (2007) 95–106, https://doi.org/10.1111/j.1460-2695.2006.01084.x.
[34] G. Meneghetti, A. Campagnolo, State-of-the-art review of peak stress method for fatigue strength assessment of welded joints, Int. J. Fatigue 139 (2020), 105705, https://doi.org/10.1016/j.ijfatigue.2020.105705.

[35] F. Scacco, U. Zerbst, G. Meneghetti, M. Madia, Comparison between PSM and IBESS approaches for the fatigue life estimation of weldments, Welding in the World 66 (2022) 1251–1273, https://doi.org/10.1007/s40194-022-01284-7.

[36] ISO. ISO 12108:2018 Metallic materials - Fatigue testing - Fatigue crack growth method 2018.

[37] Y. Si, J.P. Rouse, C.J. Hyde, Potential difference methods for measuring crack growth: A review, Int. J. Fatigue (2020) 136, https://doi.org/10.1016/j.ijfatigue.2020.105624.

[38] H.H. Johnson, Calibrating the electric potential method for studying slow crack growth, Mater. Res. Stand. (1965).

[39] H.-M. Bauschke, K.-H. Schwalbe, Measurement of the depth of surface cracks using the Direct Current Potential Drop Method, Materwiss Werksttech 16 (1985) 156–165, https://doi.org/10.1002/mawe.19850160504.

[40] S. Blasón, T. Werner, J. Kruse, M. Madia, P. Miarka, S. Seitl, et al., Determination of fatigue crack growth in the near-threshold regime using small-scale specimens, Theor. Appl. Fract. Mech. 118 (2022), 103224, https://doi.org/10.1016/j.tafmec.2021.103224.

[41] J. Maierhofer, D. Simunek, H.-P. Gänser, R. Pippan, Oxide induced crack closure in the near threshold regime: The effect of oxide debris release, Int. J. Fatigue 117 (2018) 21–26, https://doi.org/10.1016/j.ijfatigue.2018.07.021.

[42] J.C. Newman Jr., Y. Yamada, Compression precracking methods to generate near-threshold fatigue-crack-growth-rate data, Int. J. Fatigue 32 (2010) 879–885, https://doi.org/10.1016/j.ijfatigue.2009.02.030.

[43] J. Maierhofer, R. Pippan, H.-P. Gänser, Modified NASGRO equation for physically short cracks, Int. J. Fatigue 59 (2014) 200–207, https://doi.org/10.1016/j.ijfatigue.2013.08.019.

[44] P. Kucharczyk, M. Madia, U. Zerbst, B. Schork, P. Gerwien, S. Münstermann, Fracture-mechanics based prediction of the fatigue strength of weldments, Material aspects. Eng Fract Mech 198 (2018) 79–102, https://doi.org/10.1016/j.engfracmech.2017.09.010.

[45] U. Zerbst, M. Madia, Fracture mechanics based assessment of the fatigue strength: approach for the determination of the initial crack size, Fatigue Fract. Eng. Mater. Struct. 38 (2015) 1066–1075, https://doi.org/10.1111/ffe.12288.

[46] J. Qian, A. Fatemi, Mixed mode fatigue crack growth: A literature survey, Eng. Fract. Mech. 55 (1996) 969–990, https://doi.org/10.1016/S0013-7944(96)00071-9.

[47] H.A. Richard, M. Fulland, M. Sander, Theoretical crack path prediction, Fatigue Fract. Eng. Mater. Struct. 28 (2005) 3–12, https://doi.org/10.1111/j.1460-2695.2004.00855.x.

[48] M.D. Chapetti, Fracture mechanics for fatigue design of metallic components and small defect assessment, Int. J. Fatigue 154 (2022), 106550, https://doi.org/10.1016/j.ijfatigue.2021.106550.

[49] P. Lazzarin, R. Tovo, A Notch Intensity Factor Approach to the Stress Analysis of Welds, Fatigue Fract. Eng. Mater. Struct. 21 (1998) 1089–1103, https://doi.org/10.1046/j.1460-2695.1998.00097.x.

[50] P. Lazzarin, C.M. Sonsino, R. Zambardi, A notch stress intensity approach to assess the multiaxial fatigue strength of welded tube-to-flange joints subjected to combined loadings, Fatigue Fract. Eng. Mater. Struct. 27 (2004) 127–140, https://doi.org/10.1111/j.1460-2695.2004.00733.x.

[51] M.L. Williams, Stress singularities resulting from various boundary conditions in angular corners of plates in tension, J. Appl. Mech. 19 (1952) 526–528.

[52] A. Visentin, A. Campagnolo, G. Meneghetti, Analytical expressions to estimate rapidly the notch stress intensity factors at V-notch tips using the Peak Stress Method, Fatigue Fract. Eng. Mater. Struct. (2023) 1–24, https://doi.org/10.1111/ffe.13912.

[53] B. Gross, A. Mendelson, Plane elastostatic analysis of V-notched plates, Int. J. Fract. Mech. 8 (1972) 267–276, https://doi.org/10.1007/BF00186126.

[54] N. Hasebe, J. Iida, A crack originating from a triangular notch on a rim of a semi-infinite plate, Eng. Fract. Mech. 10 (1978) 773–782.

[55] A.G. Philipps, S. Karuppanan, C.M. Churchman, D.A. Hills, Crack tip stress intensity factors for a crack emanating from a sharp notch, Eng. Fract. Mech. 75 (2008) 5134–5139, https://doi.org/10.1016/j.engfracmech.2008.08.002.

[56] P. Livieri, R. Tovo, The use of the JV parameter in welded joints: Stress analysis and fatigue assessment, Int. J. Fatigue 31 (2009) 153–163, https://doi.org/10.1016/j.ijfatigue.2008.06.007.

[57] A. Carpinteri, P. Cornetti, N. Pugno, A. Sapora, D. Taylor, A finite fracture mechanics approach to structures with sharp V-notches, Eng. Fract. Mech. 75 (2008) 1736–1752, https://doi.org/10.1016/j.engfracmech.2007.04.010.

[58] A. Carpinteri, P. Cornetti, N. Pugno, A. Sapora, On the most dangerous V-notch, Int. J. Solids Struct. 47 (2010) 887–893, https://doi.org/10.1016/j.ijsolstr.2009.11.017.

[59] A. Carpinteri, P. Cornetti, A. Sapora, Brittle failures at rounded V-notches: a finite fracture mechanics approach, Int. J. Fract. 172 (2011) 1–8, https://doi.org/10.1007/s10704-011-9640-8.

[60] A. Sapora, P. Cornetti, A. Carpinteri, Cracks at rounded V-notch tips: an analytical expression for the stress intensity factor, Int. J. Fract. 187 (2014) 285–291, https://doi.org/10.1007/s10704-014-9932-x.

[61] B. Atzori, P. Lazzarin, G. Meneghetti, A unified treatment of the mode I fatigue limit of components containing notches or defects, Int. J. Fract. 133 (2005) 61–87, https://doi.org/10.1007/s10704-005-2183-0.

[62] Lazzarin P, Zambardi R. A finite-volume-energy based approach to predict the static and fatigue behavior of components with sharp V-shaped notches. International Journal of Fracture 2001 112:3 2001;112:275–98. 10.1023/A:1013595930617.

[63] H. Neuber, Kerbspannungslehre, 2nd Ed., Springer-Verlag, Berlin, 1958.

[64] P. Livieri, P. Lazzarin, Fatigue strength of steel and aluminium welded joints based on generalised stress intensity factors and local strain energy values, Int. J. Fract. 133 (2005) 247–276, https://doi.org/10.1007/s10704-005-4043-3.

[65] E. Beltrami, Sulle condizioni di resistenza dei corpi elastici (in Italian), Il Nuovo Cimento 18 (1885) 145–155.

[66] P. Lazzarin, T. Lassen, P. Livieri, A notch stress intensity approach applied to fatigue life predictions of welded joints with different local toe geometry, Fatigue Fract. Eng. Mater. Struct. 26 (2003) 49–58, https://doi.org/10.1046/j.1460-2695.2003.00586.x.

[67] M.L. Dunn, W. Suwito, S. Cunningham, Stress intensities at notch singularities, Eng. Fract. Mech. 57 (1997) 417–430, https://doi.org/10.1016/S0013-7944(97)00019-2.

[68] P. Lazzarin, R. Afshar, F. Berto, Notch stress intensity factors of flat plates with periodic sharp notches by using the strain energy density, Theor. Appl. Fract. Mech. 60 (2012) 38–50, https://doi.org/10.1016/j.tafmec.2012.06.006.

[69] R. Afshar, F. Berto, P. Lazzarin, L.P. Pook, Analytical expressions for the notch stress intensity factors of periodic V-notches under tension by using the strain energy density approach, J. Strain Anal. Eng. Des. 48 (2013) 291–305, https://doi.org/10.1177/0309324713487902.

[70] A. Sapora, P. Cornetti, A. Campagnolo, G. Meneghetti, Mode I fatigue limit of notched structures: A deeper insight into Finite Fracture Mechanics, Int. J. Fract. 227 (2021) 1–13, https://doi.org/10.1007/s10704-020-00488-6.

[71] P. Lazzarin, F. Berto, M. Zappalorto, Rapid calculations of notch stress intensity factors based on averaged strain energy density from coarse meshes: Theoretical bases and applications, Int. J. Fatigue 32 (2010) 1559–1567, https://doi.org/10.1016/j.ijfatigue.2010.02.017.

[72] P. Foti, M.R. Ayatollahi, F. Berto, Rapid strain energy density evaluation for V-notches under mode I loading conditions, Eng. Fail. Anal. 110 (2020), 104361, https://doi.org/10.1016/j.engfailanal.2019.104361.

[73] P. Foti, F. Berto, Some useful expressions and a proof of the validity of the volume free procedure for the SED method application, Eng. Fract. Mech. 274 (2022), 108818, https://doi.org/10.1016/j.engfracmech.2022.108818.

[74] P. Foti, S.M.J. Razavi, M.R. Ayatollahi, L. Marsavina, F. Berto, On the application of the volume free strain energy density method to blunt V-notches under mixed mode condition, Eng. Struct. 230 (2021), 111716, https://doi.org/10.1016/j.engstruct.2020.111716.

[75] G. Meneghetti, P. Lazzarin, The Peak Stress Method for Fatigue Strength Assessment of welded joints with weld toe or weld root failures, Welding in the World 55 (2011) 22–29, https://doi.org/10.1007/BF03321304.

[76] L. Vecchiato, A. Campagnolo, G. Meneghetti, The Peak Stress Method for fatigue lifetime assessment of fillet-welded attachments in steel subjected to variable amplitude in-phase multiaxial local stresses, Int. J. Fatigue 169 (2023), 107482, https://doi.org/10.1016/j.ijfatigue.2022.107482.

[77] A. Campagnolo, L. Vecchiato, G. Meneghetti, Multiaxial variable amplitude fatigue strength assessment of steel welded joints using the peak stress method, Int. J. Fatigue 163 (2022), 107089, https://doi.org/10.1016/j.ijfatigue.2022.107089.

[78] G. Meneghetti, A. Campagnolo, M. Avalle, D. Castagnetti, M. Colussi, P. Corigliano, et al., Rapid evaluation of notch stress intensity factors using the peak stress method: Comparison of commercial finite element codes for a range of mesh patterns, Fatigue Fract. Eng. Mater. Struct. 41 (2018) 1044–1063, https://doi.org/10.1111/ffe.12751.

[79] G. Meneghetti, A. Campagnolo, A. Visentin, M. Avalle, M. Benedetti, A. Bighelli, et al., Rapid evaluation of notch stress intensity factors using the peak stress method with 3D tetrahedral finite element models: comparison of commercial codes, Fatigue Fract. Eng. Mater. Struct. 45 (2022) 1005–1034, https://doi.org/10.1111/ffe.13645.

[80] Campagnolo A, Meneghetti G. Rapid estimation of notch stress intensity factors in 3D large-scale welded structures using the peak stress method. MATEC Web of Conferences, vol. 165, EDP Sciences; 2018. 10.1051/matecconf/201816517004.

[81] A. Campagnolo, I. Roveda, G. Meneghetti, The Peak Stress Method combined with 3D finite element models to assess the fatigue strength of complex welded structures, Procedia Struct. Integrity 19 (2019) 617–626, https://doi.org/10.1016/j.prostr.2019.12.067.

[82] C.M. Sonsino, D. Böhme, C. Kulka, R. Helwig, Slope of the S-N-Curve and high-cycle fatigue behaviour of longitudinal stiffeners in the as-welded and stress-relieved states, IIW Doc. XIII, International Institute of Welding, 1987.

[83] DIN 17100:1980. Steels for general structural purposes - Quality Standard 1980.

[84] UNI. UNI EN 10025-2:2019 - Prodotti laminati a caldo di acciai per impieghi strutturali - Parte 2: Condizioni tecniche di fornitura di acciai non legati per impieghi strutturali 2019.

[85] J. Hensel, T. Nitschke-Pagel, K. Dilger, Effects of residual stresses and compressive mean stresses on the fatigue strength of longitudinal fillet-welded gussets, Weld World 60 (2016) 267–281, https://doi.org/10.1007/s40194-015-0284-6.

[86] S. Schönborn, T. Nitschke-Pagel, Einflussgrößen auf die Lage des Abknickpunktes der Wöhlerlinie für den Schwingfestigkeitsnachweis von Schweißverbindungen (in German), DVS Forschungsvereinigung, Düsseldorf, Germany, 2014.

[87] M. Chapetti, Fatigue propagation threshold of short cracks under constant amplitude loading, Int. J. Fatigue 25 (2003) 1319–1326, https://doi.org/10.1016/S0142-1123(03)00065-3.

[88] M.D. Chapetti, T. Kitano, T. Tagawa, T. Miyata, Fatigue limit of blunt-notched components, Fatigue Fract. Eng. Mater. Struct. 21 (1998) 1525–1536, https://doi.org/10.1046/j.1460-2695.1998.00115.x.

[89] O.P. Ostash, V.V. Panasyuk, A unified model of initiation and growth of fatigue macrocracks. part 3. stage of growth of a macrocrack, Mater. Sci. 35 (1999) 299–309, https://doi.org/10.1007/BF02355474.
[90] O.P. Ostash, V.V. Panasyuk, Fatigue process zone at notches, Int. J. Fatigue 23 (2001) 627–636, https://doi.org/10.1016/S0142-1123(01)00004-4.
[91] K. Tanaka, Y. Nakai, Propagation and non-propagation of short fatigue cracks at a sharp notch, Fatigue of Engineering Materials and Structures 6 (1983) 315–327, https://doi.org/10.1111/j.1460-2695.1983.tb00347.x.
[92] S. Usami, S. Shida, Elastic-plastic analysis of the fatigue limit for a material with small flaws, Fatigue Fract. Eng. Mater. Struct. 1 (1979) 471–481, https://doi.org/10.1111/j.1460-2695.1979.tb01334.x.
[93] R. Bell, O. Vosikovsky, S. Bain, The significance of weld toe undercuts in the fatigue of steel plate T-joints, Int. J. Fatigue 11 (1989) 3–11, https://doi.org/10.1016/0142-1123(89)90041-8.
[94] J.L. Otegui, H.W. Kerr, D.J. Burns, U.H. Mohaupt, Fatigue crack initiation from defects at weld toes in steel, Int. J. Press. Vessel. Pip. 38 (1989) 385–417, https://doi.org/10.1016/0308-0161(89)90048-3.
[95] J.L. Otegui, D.J. Burns, H.W. Kerr, U.H. Mohaupt, Growth and coalescence of fatigue cracks at weld toes in steel, Int. J. Press. Vessel. Pip. 48 (1991) 129–165, https://doi.org/10.1016/0308-0161(91)90019-X.
[96] J.L. Otegui, U.H. Mohaupt, D.J. Burns, Effect of weld process on early growth of fatigue cracks in steel T joints, Int. J. Fatigue 13 (1991) 45–58, https://doi.org/10.1016/0142-1123(91)90127-K.
[97] M. Chapetti, J.L. Otegui, Importance of toe irregularity for fatigue resistance of automatic welds, Int. J. Fatigue 17 (1995) 531–538, https://doi.org/10.1016/0142-1123(95)00049-6.
[98] Engesvik KM. Analysis of uncertainties in the fatigue capacity of welded joints, Doctoral Thesis. Doctoral thesis. University of Trondheim, Division of Marine Structures, Norwegian Institute of Technology, Trondheim, Norway, 1981.
[99] K.M. Engesvik, T. Moan, Probabilistic analysis of the uncertainty in the fatigue capacity of welded joints, Eng. Fract. Mech. 18 (1983) 743–762, https://doi.org/10.1016/0013-7944(83)90122-4.
[100] S.J. Maddox, An analysis of fatigue cracks in fillet welded joints, Int. J. Fract. 11 (1975) 221–243, https://doi.org/10.1007/BF00038890.
[101] B. Schork, P. Kucharczyk, M. Madia, U. Zerbst, J. Hensel, J. Bernhard, et al., The effect of the local and global weld geometry as well as material defects on crack initiation and fatigue strength, Eng. Fract. Mech. 198 (2018) 103–122, https://doi.org/10.1016/j.engfracmech.2017.07.001.
[102] Z. Mikulski, T. Lassen, Fatigue crack initiation and subsequent crack growth in fillet welded steel joints, Int. J. Fatigue 120 (2019) 303–318, https://doi.org/10.1016/j.ijfatigue.2018.11.014.
[103] G. Wei, K. Hu, S. Chen, M. Yan, Experiment and simulation investigation of multiple cracks evolution at the weld toe, Int. J. Fatigue 144 (2021), 106037, https://doi.org/10.1016/j.ijfatigue.2020.106037.
[104] S.J. Maddox, Calculating the fatigue strength of a welded joint using fracture mechanics, Met. Constr. Br. Weld. J. 2 (1970) 327–331.
[105] Verreman Y, Bailon JP. Fatigue short crack propagation and plasticity-induced crack closure at the toe of a fillet welded joint. In: Miller KJ, de los Rios ER, editors. The Behaviour of Short Fatigue Cracks, London: EGF 1; 1986, p. 387–404.
[106] Y. Verreman, B. Nie, Short crack growth and coalescence along the toe of a manual fillet weld, Fatigue Fract. Eng. Mater. Struct. 14 (1991) 337–349, https://doi.org/10.1111/j.1460-2695.1991.tb00663.x.
[107] ANSYS Inc. Fracture Analysis Guide. 2022.
[108] C.F. Shih, B. Moran, T. Nakamura, Energy release rate along a three-dimensional crack front in a thermally stressed body, Int. J. Fract. 30 (1986) 79–102, https://doi.org/10.1007/BF00034019/METRICS.